Atmos. Meas. Tech. Discuss., https://doi.org/10.5194/amt-2018-269
Manuscript under review for journal Atmos. Meas. Tech.
Discussion started: 11 October 2018

Atmospheric Measurement Techniques Discussions

Calibration of a 35-GHz Airborne Cloud Radar: Lessons Learned and Intercomparisons with 94-GHz Cloud Radars

Florian Ewald[1], Silke Groß[1], Martin Hagen[1], Lutz Hirsch[2], Julien Delanoë[3], and Matthias Bauer-Pfundstein[4]

[1]Deutsches Zentrum für Luft und Raumfahrt, Institut für Physik der Atmosphäre, Oberpfaffenhofen, Germany
[2]Max Planck Institute for Meteorology, Hamburg, Germany
[3]LATMOS/UVSQ/IPSL/CNRS, Guyancourt, France
[4]Metek GmbH, Elmshorn, Germany

Correspondence to: Florian Ewald (florian.ewald@dlr.de)

Abstract. In this study, we will give an overview of lessons learned during the radiometric calibration of the airborne, high-power Ka-band cloud radar on board the German research aircraft HALO. Within this context, a number of flight experiments over Europe and over the tropical and extra-tropical North-Atlantic have been conducted, where the ocean surface backscatter was used as an external reference reflector. Measurements of signal linearity and signal saturation complement this characterization. To validate the external calibration, joint flights of HALO and the French Falcon 20 aircraft, which was equipped with the RASTA cloud radar at 94 GHz and underflights of the spaceborne CloudSat at 94 GHz have been conducted. Finally, the influence of different radar wavelengths was explored with numerical studies.

1 Introduction

Clouds play an important role in the climate system since they have a profound influence on Earth's radiation budget and the water cycle. Uncertainties associated with their horizontal and vertical coverage as well as their microphysics still introduce large uncertainties in climate change predictions. Depending on their characteristics, clouds can have a warming as well as a cooling effect on Earth's climate. While cirrus clouds are believed to have a net positive effect on Earth's radiation balance (Henderson et al., 2012; Hong et al., 2016), low marine stratus clouds seem to have a cooling effect (Bony and Dufresne, 2005). Although recent measurements from passive satellite sensors have given us a better picture of the global distribution of different cloud types, their behavior in a warming climate still creates the greatest uncertainty in future projections of climate (Boucher et al., 2013). In this context, the large discrepancies in retrieved cloud microphysics (Zhao et al., 2012; Stubenrauch et al., 2013) contribute to this uncertainty. In recent years, however, the deployment of cloud profiling microwave radars on the ground, on aircraft as well as on satellites, like CloudSat (Stephens et al., 2002) or the upcoming EarthCARE satellite mission (Illingworth et al., 2014), greatly advance our scientific knowledge of cloud microphysics. Like the introduction of computer tomography into medicine, cloud radar measurements opened up the internal processes in clouds to our understanding.

Nevertheless, the radiometric calibration of an airborne millimeter-wave cloud radar can be a challenging task. System parameters of transmitter and receiver system can drift due to changing ambient temperature and pressure. The radiometric

Atmos. Meas. Tech. Discuss., https://doi.org/10.5194/amt-2018-269
Manuscript under review for journal Atmos. Meas. Tech.
Discussion started: 11 October 2018

calibration is furthermore complicated for downward-looking installations on an aircraft. The missing ability of most airborne systems to point their line of site to an external reference source makes it difficult or even completely impossible to calibrate the overall system with an external reference in a laboratory.

Typically, an budget approach is used for the radiometric calibration of airborne cloud radar instruments. First, the instrument components like transmitter, receiver, waveguides, antenna and radome are characterized individually in the laboratory. During in-flight measurements, variable component parameters are then monitored and corrected for drifts using the laboratory characterization. Subsequently, all gains and losses are combined into an overall instrument calibration.

In order to meet the required radiometric accuracy and to follow good scientific practice, an external in-flight calibration becomes indispensable to check the internal calibration for systematic errors. For scanning ground-based radars, the well-defined reflectivity of calibration spheres on tethered balloons or erected trihedral corner reflectors has been a reliable external reference for years (Atlas, 2002; Sekelsky, 2002). For the airborne perspective on the other hand, the direct fly-over and the subsequent removal of additional background clutter is difficult to reproduce.

Driven by this challenge, many studies have been conducted to characterize the characteristic reflectivity of the ocean surface using microwave scatterometer-radiometer systems in the X- and Ka-band (Valenzuela, 1978; Masuko et al., 1986).

As one of the first, Caylor (1994) introduced the ocean surface backscatter technique to cross-check the internal calibration of the NASA ER-2 Doppler radar (EDOP; Heymsfield et al., 1996). In an important next step, Li et al. (2005a) combined this technique with analytical models of the ocean surface backscatter. In their work, they used circle and roll maneuvers to sample the ocean surface backscatter for different incidence angles with the Cloud Radar System (CRS; Li et al., 2004), a 94-GHz (W band) cloud radar on board the NASA ER-2 high-altitude aircraft. In this context, they proposed to point the instrument 10° off-nadir; an angle for which multiple studies found a very constant ocean surface backscatter (Durden et al., 1994; Li et al., 2005b; Tanelli et al., 2006). For this incidence angle, these studies confirmed the ocean surface to be relatively insensitive to changes in wind speed and wind direction.

Subsequent studies followed suit, applying the same technique to other airborne cloud radar instruments: the Japanese W-band Super Polarimetric Ice Crystal Detection and Explication Radar (SPIDER; Horie et al., 2000) on board the NICT Gulfstream II by Horie et al. (2004), the Ku/Ka-band Airborne Second Generation Precipitation Radar (APR-2; Sadowy et al., 2003) on board the NASA P-3 aircraft by Tanelli et al. (2006) and the W-band cloud radar (RASTA; Protat et al., 2004) on board the SAFIRE Falcon-20 by Bouniol et al. (2008).

Encouraged by these airborne studies, this in-flight calibration technique has also been proposed and successfully applied to the spaceborne CloudSat instrument (Stephens et al., 2002; Tanelli et al., 2008). Based on this success, Horie and Takahashi (2010) proposed the same technique with a whole 10° sweep across track for the next spaceborne cloud radar, the $94\,\mathrm{GHz}$ Doppler Cloud Profiling Radar (CPR) on board EarthCARE (Illingworth et al., 2014).

With CloudSat as a long term cloud radar in space, direct comparisons of radar reflectivity from ground- and airborne instruments became possible (Bouniol et al., 2008; Protat et al., 2009). While first studies still assessed the stability of the spaceborne instrument, subsequent studies turned this around by using CloudSat as a Global Radar Calibrator for ground-based or airborne radars Protat et al. (2010).

Atmos. Meas. Tech. Discuss., https://doi.org/10.5194/amt-2018-269
Manuscript under review for journal Atmos. Meas. Tech.
Discussion started: 11 October 2018

This work will focus on the internal and external calibration of the MIRA cloud radar (Mech et al., 2014) on board the German *High Altitude and Long Range Research Aircraft* (HALO), adopting the ocean surface backscattering technique described by Li et al. (2005b). In the first part, the pre-flight laboratory characterization of each instrument will be described. This includes antenna gain, component attenuation and receiver sensitivity. In a budget approach, these system parameters are then used in combination with in-flight monitored transmission and receiver noise power levels to form the internal calibration. The second part will then compare the internal calibration with external reference sources in-flight. As external reference sources, measurements of the ocean surface as well as inter-comparisons with other air- and spaceborne cloud radar instruments will be used.

This paper is organized as follows: Section 2 first introduces the cloud radar instrument and its specifications on board the HALO research aircraft. Section 3 recalls the radar equation and introduces the concept of using the ocean surface backscatter for radar calibration. The characterization and calibration of the single system components, from waveguides, antenna to belly pod is described in Section 3.1. Subsequently, the overall calibration of the radar receiver is explained in Section 3.2. Here, a central innovation of this work is the determination of the receiver sensitivity (Section 3.3 and 3.4). In the second part of the paper, the budget calibration is validated by using predicted and measured ocean surface backscatter (Section 4.3). In addition, the calibration and system performance for joint flight legs is compared to the W-band cloud radars like the airborne cloud radar RASTA (Section 5.2) and the spaceborne cloud radar CloudSat (Section 5.3).

1.1 Accuracy considerations

In order to provide scientifically sound interpretations of cloud radar measurements, a well-calibrated instrument with known sensitivity is indispensable. Many spaceborne (Delanoë and Hogan, 2008; Deng et al., 2010) or ground-borne (Donovan et al., 2000) techniques to retrieve cloud microphysics using millimeter-wave radar measurements require a well calibrated instrument. In the case of the CloudSat instrument, the calibration uncertainty was specified to be $\pm 2\,\mathrm{dB}$ or better (Stephens et al., 2002). This radiometric requirement on cloud radars for retrievals of cloud microphysics is further explained in Fig. 1. Under the simplest assumption of small, mono-disperse cloud water droplets, the iso-lines in Fig. 1 represent all combinations of cloud droplet effective radius and liquid water content with a radar reflectivity of $-20\,\mathrm{dBz}$. An increasing retrieval ambiguity, caused by an assumed instrument calibration uncertainty, is illustrated by the shaded areas with $\pm 1\,\mathrm{dB}$ (green), $\pm 3\,\mathrm{dB}$ (yellow) and $\pm 8\,\mathrm{dB}$ (red). To constrain the retrieval space considerably within synergistic radar-lidar retrievals like Cloudnet (Illingworth et al., 2007) or Varcloud (Delanoë and Hogan, 2008), the radiometric uncertainty has to be significantly smaller than the natural variability of clouds. Since a reflectivity bias of $8\,\mathrm{dB}$ would bias the droplet size by a factor of 2 and the water content by even a magnitude, the radiometric uncertainty should be at least $3\,\mathrm{dB}$ or lower. For a systematic $1\,\mathrm{dB}$ calibration offset, Protat et al. (2016) still found ice water content biases of $+19\%$ and -16% in their radar-only retrieval. Since HAMP MIRA data is used in retrievals of cloud microphysics, the target accuracy will be set to $1\,\mathrm{dB}$.

An accurate radiometric calibration is further motivated by recent studies (Protat et al., 2009; Hennemuth et al., 2008; Maahn and Kollias, 2012; Ewald et al., 2015; Lonitz et al., 2015; Myagkov et al., 2016; Acquistapace et al., 2017), which used the radar reflectivity provided by almost identical ground-based versions of the same instrument. The establishment of the MIRA

Atmos. Meas. Tech. Discuss., https://doi.org/10.5194/amt-2018-269
Manuscript under review for journal Atmos. Meas. Tech.
Discussion started: 11 October 2018

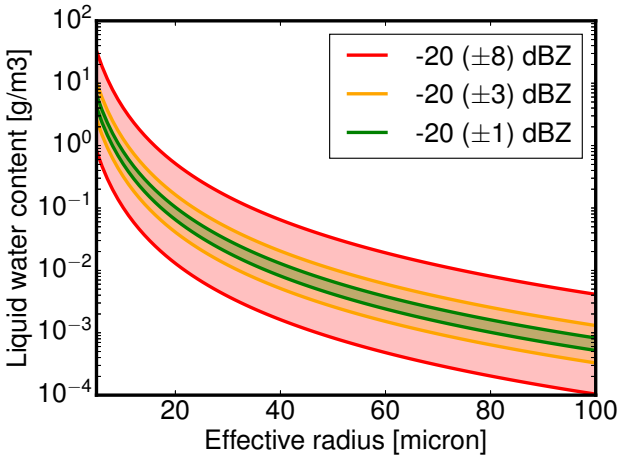

Figure 1. Microphysical retrieval uncertainty due to different radiometric calibration uncertainties (±1, ±3, $8\pm$) for monodisperse cloud water droplets according to Mie calculations.

instrument as standard instrumentation within the European Research Infrastructure for the observation of Aerosol, Clouds, and Trace gases (ACTRIS) and for Cloudnet is a further incentive for an external calibration study.

The need for an external calibration is furthermore encouraged by several studies which already found evidences of an offset in radar reflectivity when comparing different cloud radar instruments. In a direct comparison with the W-Band ($94\,\mathrm{GHz}$) ARM Cloud Radar (WACR), Handwerker and Miller (2008) found around $3\,\mathrm{dB}$ smaller reflectivities for the Karlsruhe Institute of Technology MIRA, contradicting the reflectivity reducing effect of a higher gaseous attenuation and stronger Mie scattering at $94\,\mathrm{GHz}$. Protat et al. (2009) could reproduce this discrepancy in a comparison with CloudSat, where they found a clear systematic shift of the mean vertical profile by $2\,\mathrm{dB}$ between Cloudsat and the Lindenberg MIRA (CloudSat showing higher values than the Lindenberg radar).

2 The 35-GHz cloud radar on HALO

The cloud radar on HALO is a pulsed Ka-band, polarimetric Doppler millimeter-wavelength radar which is based on prototypes developed and described by Bormotov et al. (2000) and Vavriv et al. (2004). The current system was manufactured and provided by *Metek* (Meteorologische Messtechnik GmbH, Elmshorn, Germany). The system design and its data processing, including an updated moment estimation and a target classification by Bauer-Pfundstein and Görsdorf (2007) was described in detail by Görsdorf et al. (2015). The millimeter radar is part of the HALO Microwave Package (HAMP) which will be subsequently abbreviated as *HAMP MIRA*. Its standard installation in the belly pod section of HALO with its fixed nadir-pointing $1\,\mathrm{m}$ diameter Cassegrain antenna is described in detail by Mech et al. (2014). Its transmitter is a high-power magnetron operating at $35.5\,\mathrm{GHz}$ with a peak power P_t of $27\,\mathrm{kW}$, with a pulse repetition frequency f_p between 5–$10\,\mathrm{kHz}$ and a pulse width τ_p between 100–$400\,\mathrm{ns}$. The large antenna and the high peak power give an exceptionally good sensitivity of $-47\,\mathrm{dBZ}$ for the

Atmos. Meas. Tech. Discuss., https://doi.org/10.5194/amt-2018-269
Manuscript under review for journal Atmos. Meas. Tech.
Discussion started: 11 October 2018

Atmospheric Measurement Techniques Discussions

Table 1. Technical specifications of the HAMP cloud radar as characterized in this work. Boldface indicates the operational configuration used in this work.

Parameter	Variable	Value
Wavelength	λ	8.45 mm
Pulse Power	P_t	27 kW
Pulse Repetition	f_p	**5** – 10 kHz
Pulse Width	τ_p	100, **200**, 400 ns
Recieve Window	τ_r	100, **200**, 400 ns
RF Noise Bandwidth	B_n	**7.5**, 5 MHz
RF Front-End Noise Figure	NF	9.9 dB
RF Front-End Sensitivity	P_n	−95.3 dBm
Sensitivity* (ground)	$Z_{\min}$	−47 dBZ
Sensitivity* (airborne)	$Z_{\min}$	−38 dBZ
Antenna Gain	G_a	50.0 dB
Beamwidth (3 dB)	ϕ	0.56°
Atten. (Finite Bandwith)	L_{fb}	1.2 dB
Atten. (Tx Path)	L_{rx}	0.75 dB
Atten. (Rx Path)	L_{tx}	0.75 dB
Atten. (Belly pod)	L_{bp}	1.5 dB

* at 5 km, 1 s avg., 30 m res.

ground-based operation (5 km distance, 1 s averaging and a range resolution of 30 m). The broadening of the Doppler spectrum due to the beam width reduces its airborne sensitivity to −38 dBZ as discussed in Mech et al. (2014). Table 1 lists the technical specifications as characterized in this work. Boldface indicates the operational configuration used in this work.

Most of the parameters in Table 1 play a role for the radiometric calibration of the cloud radar instrument. For this reason, this section will briefly recapitulate the conversion from receiver signal power to the commonly used radar reflectivity. Following the derivation of the meteorological form of the radar equation by Doviak and Zrnić (1993), the equivalent radar reflectivity factor $Z_e\,(\mathrm{mm^6 m^{-3}})$ can be calculated from the received signal power $P_r\,(\mathrm{W})$ by

$$Z_e = R_c P_r r^2 L_{\mathrm{atm}}^2 \tag{1}$$

where r is the range between antenna and target, L_{atm} is the one-way path integrated attenuation, and R_c is a constant which describes all relevant system parameters. Assuming a circularly symmetric Gaussian antenna pattern, this radar constant R_c contains the pulse wavelength $\lambda\,(\mathrm{m})$, pulse width $\tau_p\,(\mathrm{s})$ and peak transmit power $P_t\,(\mathrm{W})$, the peak antenna gain G_a and the antenna half-power beamwidth ϕ. It additionally accounts for waveguide losses in the transmitter L_{tx} and receiver L_{rx} path,

Atmos. Meas. Tech. Discuss., https://doi.org/10.5194/amt-2018-269
Manuscript under review for journal Atmos. Meas. Tech.
Discussion started: 11 October 2018

the loss L_{bp} in the belly pod radome and the loss L_{fb} due to the finite receiver bandwidth:

$$R_c = \frac{1024 \ln 2 \lambda^2 L_{\mathrm{tx}} L_{\mathrm{bp}}^2 L_{\mathrm{rx}} L_{\mathrm{fb}} 10^{18}}{P_t G_a^2 c \pi^3 \tau \phi^2} \tag{2}$$

Without modifications, antenna ($G_a, \phi, L_{\mathrm{bp}}$) and waveguide characteristics ($L_{\mathrm{tx}}, L_{\mathrm{bp}}^2, L_{\mathrm{rx}}$) usually have to be determined only once for each deployment. In contrast, transmitter and receiver parameters have to be monitored continuously. In addition, a thorough characterization of the receiver sensitivity is essential for the radiometric accuracy of the instrument.

3 Internal/Budget calibration

This section will discuss the internal calibration of the radar instrument and its characterization in the laboratory. The following section will then compare this budget approach in-flight with an external reference source.

The monitoring of the system specific parameters and the subsequent estimation of radar reflectivity is described in detail by Görsdorf et al. (2015). The internal calibration (budget calibration) strategy for the HAMP MIRA is therefore only briefly summarized here. In case of a deviation, previously assumed and used parameters will be given and referred as *initial calibration* for traceability of past radar measurements.

3.1 Antenna, radome and waveguides

- *Antenna*: The gain $G_a = 50.0\,\mathrm{dBi}$ and the beam pattern ($-3\,\mathrm{dB}$ beamwidth $\phi = 0.56\,°$) was determined by the manufacturer by installing the $1\,\mathrm{m}$ diameter Cassegrain antenna on a pedestal to scan its pattern on a tower 400 meters away. The antenna pattern showed no obvious asymmetries or increased sidelobes (sidelobe level: $-22\,\mathrm{dB}$). Its characterization revealed no significant differences in comparison with the initially estimated parameters ($G_a = 49.75\,\mathrm{dBi}$, $\phi = 0.6\,°$).

- *Radome*: The thickness of the epoxy quartz radome in the belly pod was designed with a thickness of $4.53\,\mathrm{mm}$ to limit the one-way attenuation to around $0.5\,\mathrm{dB}$. Deviations during manufacturing increased the thickness to $4.84\,\mathrm{mm}$, with a one-way attenuation of around $1.5\,\mathrm{dB}$. Laboratory measurements confirmed this $2.0\,\mathrm{dB}$ ($2 \times 1.0\,\mathrm{dB}$) higher two-way attenuation compared to the initially used value for the radome attenuation.

- *Waveguides*: The initially used calibration did not accounted for the losses caused by the longer waveguides in the airplane installation. Actually, transmitter and receiver waveguides each have a length of $1.15\,\mathrm{m}$. With a specified attenuation of $0.65\,\mathrm{dB/m}$, the two-way attenuation by waveguides is thus $1.5\,\mathrm{dB}$.

3.2 Transmitted and received signal power

- *Transmitter peak power* P_t: Due to strong variations in ambient temperatures in the cabin, in-flight thermistor measurements proved to be unreliable. For this reason, thermally stabilized measurements of P_t were conducted on ground which were correlated with measured magnetron currents I_m. The relationship between both parameters then allowed to derive P_t from in-flight measurements of I_m.

Atmos. Meas. Tech. Discuss., https://doi.org/10.5194/amt-2018-269
Manuscript under review for journal Atmos. Meas. Tech.
Discussion started: 11 October 2018

Atmospheric Measurement Techniques Discussions

– *Finite receiver bandwidth loss* L_{fb}: The loss caused by a finite receiver bandwidth was discussed in detail by Doviak and Zrnić (1979). For a Gaussian receiver response, the finite receiver bandwidth loss L_{fb} can be estimated using

$$L_{\mathrm{fb}} = -10\log_{10}\left(\coth(2b) - \frac{1}{2b}\right) \quad \text{with:} \quad b = \frac{\pi B_6 \tau_p}{4\sqrt{\ln 2}} \tag{3}$$

Here, B_6 is the $6\,\mathrm{dB}$ filter bandwidth of the receiver and τ_p is the duration of the pulse. During the initial calibration, no correction of the finite receiver bandwidth loss was applied.

– *Signal-to-Noise* (SNR): By a real-time Fast Fourier Transformation, MIRA's digital receiver converts the phase shift of consecutive pulse trains ($N_{\mathrm{FFT}} = 256$) into power spectra of Doppler velocities v_i. Subsequently, the signals $S_r(v_i)$ in the single velocity bins are summed to yield the total received signal in each gate:

$$S_r = \sum_{i=1}^{\mathrm{NFFT}} S_r(v_i) \tag{4}$$

The receiver chain omits a separate absolute power meter circuit. At the end of each pulse cycle, the receiver is switched to internal reference gates by a pin diode in front of the first amplifier. These two last gates are called the receiver noise gate and the calibration gate. In that way, a signal-to-noise ratio is calculated by dividing the signal S_r received in each atmospheric gate by the signal S_{ng} measured in the noise gate:

$$\mathrm{SNR}^{\dagger} = \frac{S_r}{S_{\mathrm{ng}}} \tag{5}$$

The relative power of the calibration gate to the receiver noise gate is furthermore used to monitor the receiver sensitivity (for details see Sec. 3.3). The main advantage of this method is the simultaneous monitoring of the relative receiver sensitivity using the same circuitry that is used for atmospheric measurements. Furthermore, the determination of the receiver noise in a separate noise gate can prevent biases in SNR, when the noise floor in atmospheric gates is obscured by aircraft motion or strong signals, both leading to a broadened Doppler spectrum.

– *Received signal power* P_r: The SNR response of the receiver to an input power P_r is described by a receiver transfer function $\mathrm{SNR} = \mathcal{T}(P_r)$. When $\mathcal{T}$ is known, an unknown received signal power P_r can be derived from a measured SNR by the inversion $\mathcal{T}^{-1}$:

$$P_r = \mathcal{T}^{-1}(\mathrm{SNR}) \approx P_n\,\mathrm{SNR} \tag{6}$$

– *Receiver sensitivity* P_n: For a linear receiver, $\mathcal{T}^{-1}$ can be approximated by a signal-independent receiver sensitivity P_n, which translates a measured SNR to an absolute signal power P_r in dBm. More specifically, P_n can be interpreted as an overall receiver noise power and is thus equal to the power of the smallest measurable white signal. It includes the inherent thermal noise within the receiver response, the overall noise figure of the receiver and mixer circuitry and all losses occurring between ADC and receiver input.

Atmos. Meas. Tech. Discuss., https://doi.org/10.5194/amt-2018-269
Manuscript under review for journal Atmos. Meas. Tech.
Discussion started: 11 October 2018

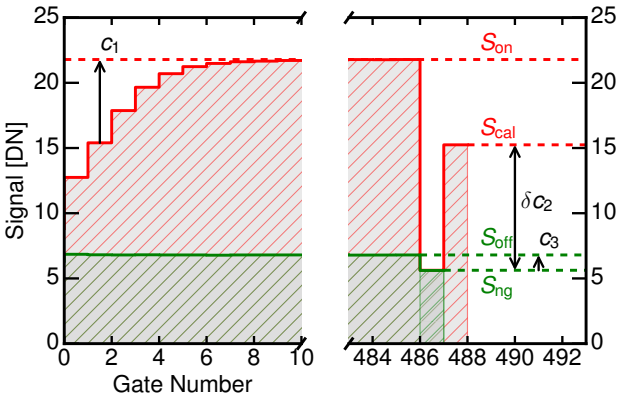

Figure 2. Received signal S as a function of gate number with external noise source switched on (S_{on}, red) and switched off (S_{off}, green). The two last gates monitor the signals S_{ng} and S_{cal}, which correspond to the receiver noise and the internal calibration source. The factors c_1, c_2 and c_3 correct the estimated noise power $P_n^\dagger$ to reflect the actual receiver sensitivity P_n.

3.3 Estimated Receiver Sensitivity

Prior to this work, no rigorous determination of the receiver transfer function $\mathcal{T}$ was performed. During the initial calibration, the receiver sensitivity P_n was instead estimated using the inherent thermal noise and its own noise characteristic.

Generated by thermal electrons, the inherent noise power $P_n^\dagger$ received by a matched receiver can be derived using Boltzmann's constant k_B, temperature T_0 and the noise bandwidth B_n of the receiver. Additional noise power is introduced by the electronic circuitry itself, which is considered by the receiver noise factor F_n or by the receiver noise figure NF in decibels.

$$P_n^\dagger = k_B T_0 B_n F_n \quad [W] \tag{7}$$

Using a calibrated external noise source with known excess noise ratio (ENR), F_n was determined in the laboratory. In-flight, F_n is monitored using the calibration and the noise gate.

In the following, measurements obtained with the calibrated external noise source in the lab are marked with an asterisk. Fig. 2 shows the external noise source measurements, where the received signal S is plotted as a function of the gate number. While connected to the receiver input, the external noise source is switched on and off with signals $S^*_{\mathrm{on}}(r)$ (red) and $S^*_{\mathrm{off}}(r)$ (green) measured in atmospheric gates. Corresponding to this, S^*_{cal} and S^*_{ng} are the signals measured in the two last gates, namely the calibration and the receiver noise gates. The in-flight signals in these two reference gates are denoted by S_{cal} and S_{ng}.

Using the so called *Y factor method*, the averaged noise floor ratio Y in atmospheric gates between the external noise source being switched on and off and the ENR of the external noise source are used to determine the noise factor F_n created by the receiver components:

$$F_n = \frac{\mathrm{ENR}}{Y-1} \quad \text{with} \quad Y = \frac{\langle S^*_{\mathrm{on}}(r)\rangle}{\langle S^*_{\mathrm{off}}(r)\rangle} \tag{8}$$

Atmos. Meas. Tech. Discuss., https://doi.org/10.5194/amt-2018-269
Manuscript under review for journal Atmos. Meas. Tech.
Discussion started: 11 October 2018

Here, the averaging $\langle S^*_{\mathrm{on}}(r)\rangle$ of atmospheric gates is done for gate numbers larger 10 to exclude the attenuation caused by the transmit/receive switch immediately after the magnetron pulse. During the initial calibration with the external noise source, a noise figure NF $= 8.8\,\mathrm{dB}$ was determined.

Summarizing the above considerations, an overall receiver sensitivity $P_n^\dagger$ is estimated using an assumed receiver noise bandwidth of $5\,\mathrm{MHz}$, a receiver temperature of $290\,\mathrm{K}$ and a noise figure of NF $= 8.8\,\mathrm{dB}$. According to Eq. 7, the estimated receiver sensitivity $P_n^\dagger$ used in the initial calibration is

$$P_n^\dagger = -98.2 \quad [\mathrm{dBm}] \tag{9}$$

The measurements with the external noise source are furthermore exploited to correct for various effects, which cause deviations between the inherent noise power $P_n^\dagger$ in the noise gate and the actual receiver sensitivity P_n:

$$P_n = c_1 c_2 P_n^\dagger \tag{10}$$

Here,

- c_1 accounts for the attenuation in atmospheric gates, which is caused by the transmit/receive switch immediately after the magnetron pulse:

  $$c_1(r) = \frac{\langle S^*_{\mathrm{on}}(r) - S^*_{\mathrm{off}}(r)\rangle}{S^*_{\mathrm{on}}(r) - S^*_{\mathrm{off}}(r)} \tag{11}$$

  As evident in Fig. 2, c_1 is only significant in the first 8 range gates ($= 240\,\mathrm{m}$) and rapidly converges to $0\,\mathrm{dB}$ in the remaining atmospheric and reference gates.

- Secondly, the correction factor c_2 is used to monitor and correct in-flight drifts in the receiver sensitivity. For this, the ratio $S^*_{\mathrm{cal}}/S^*_{\mathrm{ng}}$ measured during calibration between calibration and noise gate is compared to the ratio $S_{\mathrm{cal}}/S_{\mathrm{ng}}$ during flight:

  $$c_2 = \frac{S^*_{\mathrm{cal}}/S^*_{\mathrm{ng}}}{S_{\mathrm{cal}}/S_{\mathrm{ng}}} \tag{12}$$

- A further factor accounts for the fact that the noise level measured in the noise gate is lower than the total system noise with matched load because the low-noise amplifier is not matched during the noise gate measurement. The signal-to-noise SNR† determined with the noise gate level therefore overestimates the actual signal-to-noise SNR in atmospheric gates:

  $$\mathrm{SNR} = c_3 \mathrm{SNR}^\dagger \tag{13}$$

  In Fig. 2, this offset is called c_3. Its value is determined by comparing the signal S^*_{ng} in the noise gate with the signal S^*_{off} in atmospheric gates, while the external noise source is switched off:

  $$c_3 = \frac{S^*_{\mathrm{ng}}}{S^*_{\mathrm{off}}} \tag{14}$$

  This offset between noise gate and total system noise remains very stable with $c_3 = -0.83\,\mathrm{dB}$.

Atmos. Meas. Tech. Discuss., https://doi.org/10.5194/amt-2018-269
Manuscript under review for journal Atmos. Meas. Tech.
Discussion started: 11 October 2018

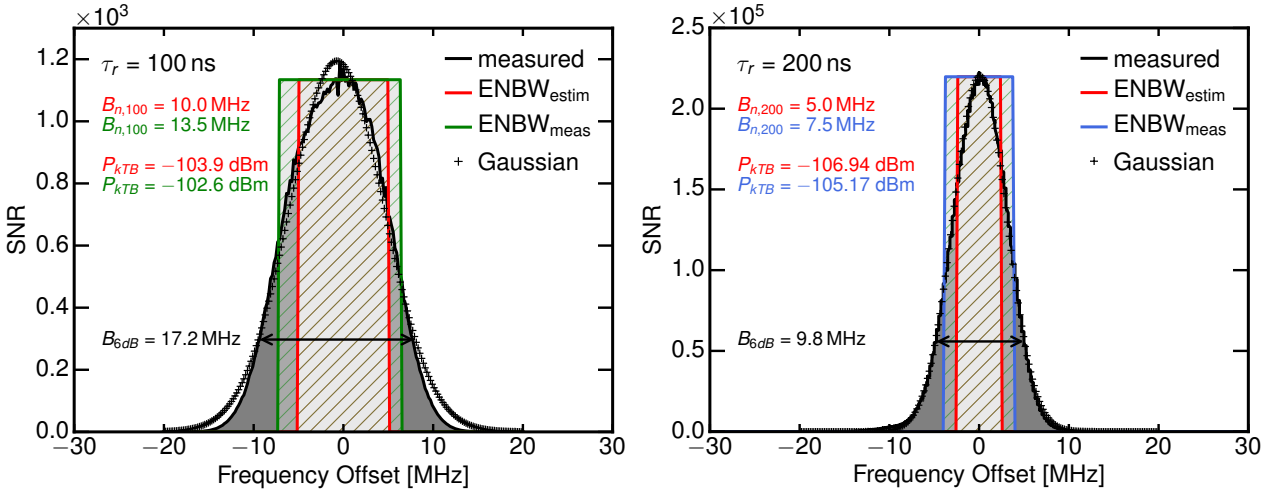

Figure 3. Measured radar receiver response (gray) as a function of the frequency offset from the center frequency at 35.5 GHz for two different receive window lengths. While the green and blue hatched rectangles show the actual equivalent noise bandwidths, the red-hatched rectangles show the estimated noise bandwidth that was used in the initial calibration.

3.4 Measured Receiver Sensitivity

A key component of this work was to replace the estimated receiver sensitivity $P_n^\dagger$ with an actual measured value P_n. While $P_n^\dagger$ was calculated using an estimated receiver noise bandwidth and the receiver noise factor, P_n is now measured directly using a calibrated signal generator with adjustable power and frequency output. By varying the power at the receiver input, P_n is found as the noise equivalent signal when SNR $= 0$. In additon, the receiver response and its bandwidth is determined by varying the frequency of the signal generator. Both measurements are then used to evaluate and check F_n according to Eq.7. This is done for two different receive window lengths ($\tau_r = 100\,\mathrm{ms}$, $\tau_r = 200\,\mathrm{ms}$) to characterize the dependence of B_n and F_n on τ_r.

To this end, an analog continuous wave signal generator *E8257D* from *Agilent Technologies* was used to determine the receiver's spectral response and its power transfer function $\mathcal{T}$. The signal generator was connected to the antenna port of the radar receiver and tuned to 35.5 GHz, the central frequency of the local oscillator. For the characterization, the radar receiver was set into standard airborne operation mode. In this mode, 256 samples are averaged coherently into power spectra by FFT. Subsequently, 20 power spectra are then averaged to obtain a smoothed power spectrum for each second.

3.4.1 Receiver Bandwidth

To determine the spectral response, the frequency sweep mode of the signal generator with a fixed signal amplitude was used within a region of $35500 \pm 20\,\mathrm{MHz}$. For the longer receive window on the left and the shorter receive window on the right, Fig. 3 shows measured signal-to-noise ratios as a function of the frequency offset from the center frequency at 35.5 GHz. The spectral receiver response for both receive windows (black lines) approaches a Gaussian fit (crosses). To estimate the finite receiver

Atmos. Meas. Tech. Discuss., https://doi.org/10.5194/amt-2018-269
Manuscript under review for journal Atmos. Meas. Tech.
Discussion started: 11 October 2018

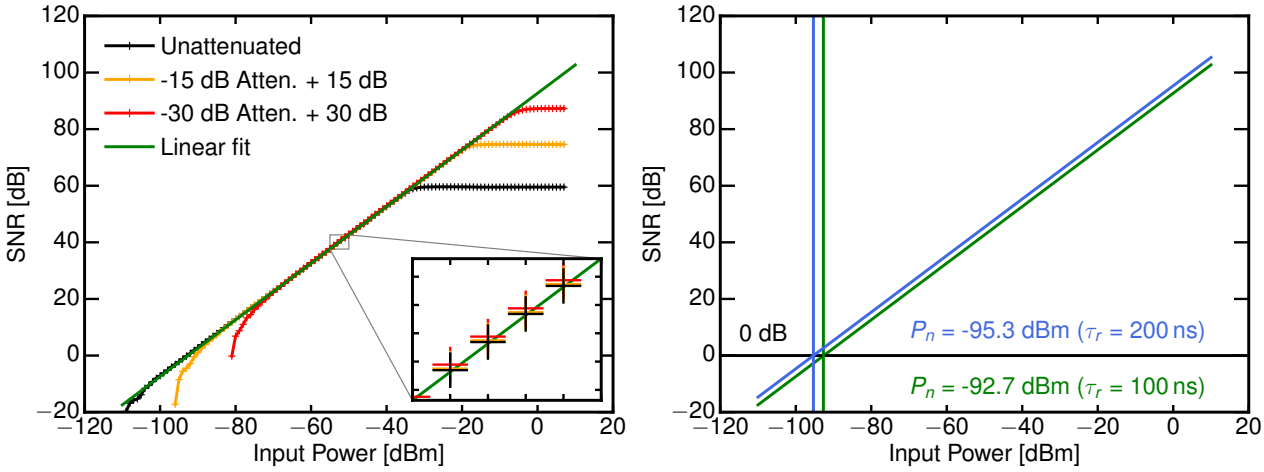

Figure 4. (left) Measured receiver transfer functions for the three attenuator settings of $0\,\mathrm{dB}$ (black), $15\,\mathrm{dB}$ (green) and $30\,\mathrm{dB}$ (red). **(right)** Linear regression receiver transfer function to determine the receiver sensitivity P_n.

bandwidth loss L_{fb} using Eq. 3, the $6\,\mathrm{dB}$ filter bandwidth (orange line) is determined directly from the receiver response with $B_6 = 9.8\,\mathrm{MHz}$ for $\tau_r = 200\,\mathrm{ms}$ and $B_6 = 17.2\,\mathrm{MHz}$ for $\tau_r = 100\,\mathrm{ms}$, respectively. In the following, the equivalent noise bandwidth (ENBW) concept is used to determine the receiver noise bandwidth B_n which is needed to calculate P_n In short, the ENBW is the bandwidth of a rectangular filter with the same received power as the actual receiver. Illustrated by the green and blue hatched rectangles in Fig. 3, the measured ENBW is $B_{n,200} = 7.5\,\mathrm{MHz}$ for the longer receive window and $B_{n,100} = 13.5\,\mathrm{MHz}$ for the shorter receive window. In contrast, the red-hatched rectangles show the estimated $5\,\mathrm{MHz}$ (resp. $10\,\mathrm{MHz}$) receiver noise bandwidth using $1/\tau_r$. The discrepancy between the measured and the estimated noise bandwidth could be traced back to an additional window function which was applied unintentionally to IQ data within the digital signal processor. This issue lead to a bit more thermal noise. For the operationally used receive window length $\tau_r = 200\,\mathrm{ms}$, the offset between estimated and actual thermal noise level ($106.9\,\mathrm{dBm}$ vs. $-105.2\,\mathrm{dBm}$) lead to an underestimation of radar reflectivity of $1.8\,\mathrm{dB}$. Future measurements will not include this bias since this issue was found and fixed.

3.4.2 Receiver Transfer Function

Next, the amplitude ramp mode of the signal generator was used to determine the transfer function $P_r = \mathcal{T}(\mathrm{SNR})$ of the receiver. The receiver transfer function references absolute signal powers at the antenna port with corresponding SNR values measured by the receiver. Moreover, the linearity and cut-offs of the receiver can be assessed on the basis of the transfer function. For this measurement, the frequency of the signal generator was set to $35.5\,\mathrm{GHz}$, while the output power of the generator was increased steadily from $-110\,\mathrm{dBm}$ to $10\,\mathrm{dBm}$. This was done in steps of $1\,\mathrm{dBm}$ while averaging over 10 power spectra. In order to test the linearity and the saturation behavior of the receiver for strong signals, this measurements were repeated with an internal attenuator set to $15\,\mathrm{dB}$ and $30\,\mathrm{dB}$. For $\tau_r = 200\,\mathrm{ms}$, Fig. 4a shows the measured receiver transfer

Atmos. Meas. Tech. Discuss., https://doi.org/10.5194/amt-2018-269
Manuscript under review for journal Atmos. Meas. Tech.
Discussion started: 11 October 2018

Atmospheric Measurement Techniques Discussions

functions for the three attenuator settings of $0\,\mathrm{dB}$ (black), $15\,\mathrm{dB}$ (green) and $30\,\mathrm{dB}$ (red). For measurements with activated attenuator, SNR values have been corrected by $+15\,\mathrm{dB}$ (respectively $+30\,\mathrm{dB}$) to compare the transfer functions to the one with $0\,\mathrm{dB}$ attenuation. The overlap of the different transfer functions between input powers of $-70\,\mathrm{dBm}$ and $-30\,\mathrm{dBm}$ in Fig. 4a confirms the specified attenuator values of $15\,\mathrm{dB}$ and $30\,\mathrm{dB}$. Furthermore, no further saturation by additional receiver components (e.g. mixers or filters) can be detected up to an input power of $-5\,\mathrm{dBm}$. This allows to shift the dynamic range by using the attenuator to measure higher input powers (which would otherwise be saturated) without loosing the absolute radiometric calibration. This feature is essential for the evaluation of very strong signals like the ground return.

Subsequently, a linear regression to the results without attenuator was performed between input powers of $-70\,\mathrm{dBm}$ and $-40\,\mathrm{dBm}$, which is shown in Fig. 4b.

$$\mathrm{SNR} = \mathcal{T}(P_r) \approx mP_r - P_n \quad [dB] \tag{15}$$

With a slope m of $1.0009\,(\pm 0.0006)$ and a residual of $0.054\,\mathrm{dB}$, the receiver behaved very linearly for this input power region. Similar values were obtained for an attenuation of $+15\,\mathrm{dB}$ with a slope of $0.9980\,(\pm 0.0005)$ and a residual of $0.024\,\mathrm{dB}$ and a slope of $0.9884\,(\pm 0.0013)$ and a residual of $0.1\,\mathrm{dB}$ for an attenuation of $+30\,\mathrm{dB}$.

3.4.3 Receiver Sensitivity

Finally, the linear regression to the receiver transfer function can be used to derive the receiver sensitivity P_n. Its x-intercept ($\mathrm{SNR} = 0$) directly yields the receiver sensitivity $P_n$for the two receive window lengths:

$$P_n = -92.7\,\mathrm{dBm} \qquad (\tau_r = 100\,\mathrm{ms}) \tag{16}$$

$$P_n = -95.3\,\mathrm{dBm} \qquad (\tau_r = 200\,\mathrm{ms}) \tag{17}$$

As discussed before, the setting with the shorter receive window collects more thermal noise due to the larger receiver bandwidth. In a final step, this top-down approach to obtain P_n for different τ_r can be used to determine F_n and check for its dependence on τ_r. By solving Eq. 7 for F_n and inserting the measured bandwidths B_{100} and B_{200} we obtain:

$$P_n \,/\, P_{kTB} = F_n \tag{18}$$

$$-92.7\,\mathrm{dBm} + 102.6\,\mathrm{dBm} = 9.9\,\mathrm{dB} \qquad (\tau_r = 100\,\mathrm{ms}) \tag{19}$$

$$-95.3\,\mathrm{dBm} + 105.2\,\mathrm{dBm} = 9.9\,\mathrm{dB} \qquad (\tau_r = 200\,\mathrm{ms}) \tag{20}$$

Remarkably, F_n shows no dependence on τ_r but turns out to be larger than previsouly estimated by $1.1\,\mathrm{dB}$.

3.5 Overall calibration budget

Comparing the measured $P_n = -95.3\,\mathrm{dBm}$ to the estimated $P_n^{\dagger} = -98.2\,\mathrm{dBm}$ for $\tau_r = 200\,\mathrm{ms}$, the combination of bandwidth bias ($1.8\,\mathrm{dB}$) and larger noise figure ($1.1\,\mathrm{dB}$) caused an radar reflectivity underestimation of $2.9\,\mathrm{dB}$. Combined with the non-application of the $2.0\,\mathrm{dB}$ higher two-way attenuation by the radome, the $1.5\,\mathrm{dB}$ higher two-way attenuation by the waveguides

Atmos. Meas. Tech. Discuss., https://doi.org/10.5194/amt-2018-269
Manuscript under review for journal Atmos. Meas. Tech.
Discussion started: 11 October 2018

Atmospheric Measurement Techniques Discussions

Table 2. Breakdown of the offset between original and new calibration for each system parameter. Values for $L_{\mathrm{rx+tx}}$ and L_{fb} were already known but not applied in past measurement campaigns. The total offset has to be applied to R_c and Z.

Parameter	Original	This study	Offset
$L_{\mathrm{rx+tx}}$	-	1.5 dB	+1.5 dB
L_{fb}	-	1.2 dB	+1.2 dB
L^2_{bp}	1.0 dB	3.0 dB	+2.0 dB
G_{a}	49.75 dBi	50.0 dBi	-0.5 dB
ϕ_{a}	0.6°	0.56°	+0.6 dB
P_n	-98.2 dBm	-95.3 dBm	
NF	8.8 dB	9.9 dB	+1.1 dB
B_n	5 MHz	7.5 MHz	+1.8 dB
Total			+7.6 dB

and including the finite receiver bandwidth loss $L_{\mathrm{fb}} = 1.2\,\mathrm{dB}$, radar reflectivity derived with the initial calibration has to be corrected by $+7.6\,\mathrm{dB}$. Table 2 summarizes and breaks down all offsets found in this work.

4 External calibration using the ocean surface backscatter

The following section will now test the radiometric calibration using an external reference target. As already mentioned in the introduction, the ocean surface has been used as a calibration standard for air- and spaceborne radar instruments. In their studies, Barrick et al. (1974) and Valenzuela (1978) reviewed and harmonized theories to describe the interaction of electromagnetic waves with the ocean surface. They showed that the normalized radar cross-section σ_0 of the ocean surface at small incidence angles ($\Theta < 15\,°$) can be described by quasi-specular scattering theory. At larger incidence angles ($\Theta > 15\,°$), Bragg scattering at capillary waves becomes dominant, which complicates and enhances the backscattering of microwaves by ocean waves.

4.1 Modeling the normalized radar cross-section of the ocean surface

At the scales of millimeter waves and for small incidence angles θ, the ocean surface slope distribution is assumed to be Gaussian and isotropic, where the surface mean square slope $s(v)$ is a sole function of the wind speed v and independent from wind direction. Backscattered by ocean surface *facets*, which are aligned normal to the incidence waves (Plant, 2002), the normalized radar cross-section σ_0 can be described as a function of ocean surface wind speed v and beam incidence angle θ (Valenzuela, 1978; Brown, 1990; Li et al., 2005b):

$$\sigma_0(v,\theta,\lambda) = \frac{|\Gamma_e(0,\lambda)|^2}{s(v)^2\cos^4(\theta)} \exp\left[-\frac{\tan^2(\theta)}{s(v)^2}\right] \tag{21}$$

For the ocean surface facets at normal incidence, the reflection of microwaves is described by an effective Fresnel reflection coefficient $\Gamma_e(0,\lambda) = C_e \frac{[n(\lambda)-1]}{[n(\lambda)+1]}$. In this study, the complex refractive index $n(\lambda = 8.8\,\mathrm{mm}) = 5.565 + 2.870i$ for seawater at $25\mathrm{C}$ is used following the model by Klein and Swift (1977). Like with other models (Ray, 1972; Meissner and Wentz, 2004), the impact of salinity on σ_0 is negligible, while the influence of the ocean surface temperature on σ_0 stays below $\Delta\sigma_0 = 0.5\,\mathrm{dB}$ between $5\,^\circ\mathrm{C}$ and $30\,^\circ\mathrm{C}$. Since specular reflection is only valid in the absence of surface roughness, various studies (Wu, 1990; Jackson, 1992; Freilich and Vanhoff, 2003; Li et al., 2005a) included an *correction factor* C_e to describe the reflection of microwaves on wind-roughened water facets. While C_e has been well characterized for the Ku-band (Apel, 1994; Freilich and Vanhoff, 2003) and W-band (Horie et al., 2004; Li et al., 2005a), experimental results valid for the Ka-band are scarce (Nouguier et al., 2016). Tanelli et al. (2006) used simultaneous measurements of σ_0 in the Ku- and Ka-band, to determine $|\Gamma_e(0,\lambda = 8.8\mathrm{mm})|^2 = 0.455$ for the Ka-band, which corresponds to a correction factor C_e of 0.90. However, there is an ongoing discussion about an influence of radar wavelength or wind speed on C_e (Jackson, 1992; Tanelli et al., 2008). Chen et al. (2000) explains this disagreement with the different surface mean square slope statistics used in these studies, which do not include ocean surface roughness at the millimeter scale. To include this uncertainty in this study, the correction factor C_e has been varied between 0.85 and 0.95, while the simple model for non-slick ocean surfaces by Cox and Munk (1954) was used for $s(v)$. In their model, the surface mean square slope $s(v)$ scales linearly with wind speed v, describing a smooth ocean surface including gravity and capillary waves:

$$s(v) = 0.003 + 5.08\mathrm{e}{-3}v \tag{22}$$

4.2 Measuring the normalized radar cross-section of the ocean surface

The ocean surface backscatter is also measured by the Global Precipitation Measurement (GPM; Hou et al., 2013) platform which carries a Ku-/Ka-band dual-frequency precipitation radar (KaPR). For this study, σ_0^* from GPM is used as an independent source to support the calculated σ_0 from the model. Operating at $35.5\,\mathrm{GHz}$, the KaPR scans the surface backscatter with its 0.7° beamwidth phased array antenna resulting in a $120\,\mathrm{km}$ swath of $5\,\mathrm{km} \times 5\,\mathrm{km}$ footprints. The measured ocean surface backscatter by GPM is operationally used to retrieve surface wind conditions and path-integrated attenuation of the radar beam. In the following, the σ_0^* corrected for gaseous attenuation from GPM was used which corresponds to the co-localized matched swath of the KaPR.

During the second *Next Generation Remote Sensing for Validation Studies* (NARVAL2) in June-August 2016, HAMP MIRA was deployed on HALO. The campaign was focused on the remote sensing of organized convection over the tropical North Atlantic Ocean in the vicinity of Barbados. Another campaign objective was the integration and validation of the new remote sensing instruments on board the HALO aircraft. For the HAMP MIRA cloud radar, multiple roll- and circle-maneuvers at different incidence angles were included in research flights to implement the well established calibration technique to measure the normalized radar cross-section of the ocean surface at different incidence angles.

During NARVAL2, HAMP MIRA was installed in the belly pod section of HALO and aligned in a fixed nadir-pointing configuration with respect to the airframe. The incidence angle is therefore controlled by pitch-and-roll maneuvers of the aircraft. The aircraft position and attitude are provided at a $10\,\mathrm{Hz}$ rate by the *BAsic HALO Measurement And Sensor System*

(BAHAMAS; Krautstrunk and Giez, 2012). Pitch, roll and yaw angles are provided with an accuracy of $0.05\,°$, while the absolute uncertainty can be up to $0.1\,°$. Additional incidence angle uncertainty is caused by uncertainties in the alignment of the radar antenna. Following the approach of Haimov and Rodi (2013), the apparent Doppler velocity of the ground was used to determine the antenna beam-pointing vector. With this technique, the offsets from nadir with respect to the airframe was determined with $0.5\,°$ to the left in roll direction and $0.05\,°$ forward in pitch direction.

During calibration patterns, HALO flew at $9.7\,\mathrm{km}$ altitude with a ground speed of $180\,\mathrm{ms}^{-1}$ to $200\,\mathrm{ms}^{-1}$. The pulse repetition frequency was kept at $5\,\mathrm{kHz}$ with a pulse length of $\tau_p = 200\,\mathrm{ns}$. For the purpose of calibration, the data processing and averaging was set to $1\,\mathrm{Hz}$, being the standard campaign setting with Doppler spectra averaged from 20 FFTs which each contain 256 pulses. As a consequence of this configuration, the ocean surface backscatter at nadir was sampled in gates measuring approx $100\,\mathrm{m}$ in the horizontal and $30\,\mathrm{m}$ in the vertical. With this gate geometry, a uniform beam-filling of the ocean surface is ensured for incidence angles below $20\,°$.

In the current configuration, the point target spread function of the matched receiver is under-sampled since the sampling is matched to the gate length. Thus, the maximum of the ocean backscatter can become underestimated when the surface is located between two gates. At nadir incidence, negative bias of σ_0 of up to $3-4\,\mathrm{dB}$ were observed in earlier measurement campaigns, when the gate spacing equals or is larger than the pulse length (Caylor et al., 1997). For this reason, the received power from the range gates below and above were added to the received power of the strongest surface echo. By adding the power from only three gates, Caylor et al. (1997) could reduce the uncertainty in σ_0 to $1\,\mathrm{dB}$ and exclude the contribution by antenna side-lobes from larger ranges.

Furthermore, the backscattered signal was corrected for gaseous attenuation by oxygen and water vapor considered in the loss factor L_{atm}. While the two-way attenuation by oxygen and water vapor is normally almost negligible in the Ka-band, it has to be considered in subtropical regions with high humidity and temperature near the surface. To this end, the gaseous absorption model for millimeter waves by Rosenkranz (1998) was used. Sounding profiles of pressure, temperature and humidity were provided by *Vaisala RD-94* dropsondes, which were launched from HALO during the calibration maneuvers.

Following Li et al. (2005a), the measured normalized cross-section σ_0^* of the ocean surface can be calculated from measured signal-to-noise-ratios:

$$\sigma_0^* = \frac{c\pi^5 \tau R_c r^2 L_{\mathrm{atm}}^2}{2\lambda^4 10^{18}} P_n \mathrm{SNR} \tag{23}$$

Here, the receiver power P_r was replaced by P_nSNR (Eq. 6) to include the overall receiver sensitivity P_n in the formulation of σ_0^*. Like in Eq. 1, R_c is the radar constant which includes the transmitter power P_t, transmitting and receiving waveguide loss L_{tx} and L_{rx}, attenuation by the belly pod L_{bp} and the antenna gain G_a. Together with P_n, the combination of these system parameters are being checked in the following section, when the measured σ_0^* is compared to the modeled σ_0.

4.3 Comparison of measurements and model

The HAMP MIRA calibration maneuver during NARVAL2 was included into research flight RF03 on 12 August 2016. The flight took place $700\,\mathrm{km}$ east from Barbados in a region of a relatively pronounced dry intrusion with light winds and very

Atmos. Meas. Tech. Discuss., https://doi.org/10.5194/amt-2018-269
Manuscript under review for journal Atmos. Meas. Tech.
Discussion started: 11 October 2018

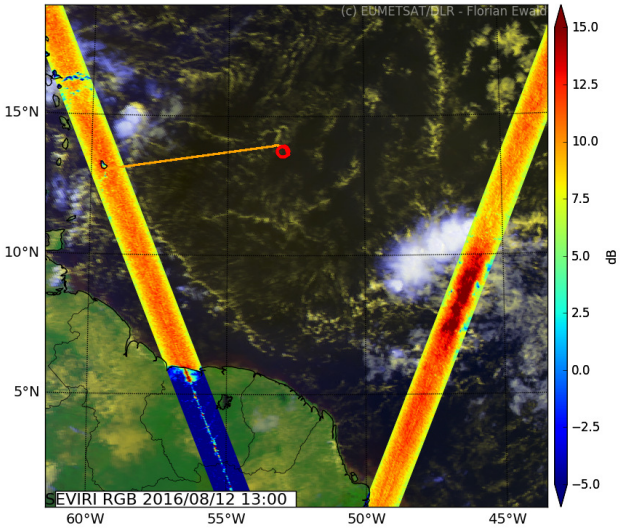

Figure 5. Flight track in orange with a true color image taken during that time by the geostationary SEVIRI instrument. The superimposed color-map shows the Ka-band σ_0^* measured by GPM in the vicinity of the operating area.

little cloudiness. Fig. 5 shows the flight track in orange with a true color image taken during that time by the geostationary SEVIRI instrument. The superimposed color-map shows σ_0^* from GPM in the vicinity of the operating area for that day. Here, the satellite nadir is located in the center of each track, with inclination angles $\theta > 0$ left and right towards the edges of the swath. Apparently, σ_0^* seems spatially quite homogeneous, where the ocean surface is only covered by small marine cumulus clouds. The first way-point was chosen to be collocated with a meteorological buoy ($14.559\,°N, 53.073\,°W$, NDBC 41040) to obtain the accurate wind-speed and direction at the level of the ocean surface as well as wave heights measured by the buoy. At $12:50$ UTC, the buoy measured a wind-speed of $5.7\,\mathrm{m/s}$ from $98\,°$ with a mean wave height of $1\,\mathrm{m}$ and mean wave direction of $69\,°$. A detailed overview of the flight path during the calibration maneuver is shown in Fig. 6, where the beam incidence angle θ is shown by the color-map. At $12:40$ UTC, the aircraft executed a set of $\pm 20\,°$ roll maneuvers to sample σ_0^* in the cross-wind direction. At $12:44$ UTC, the aircraft entered a right-hand turn with a constant roll angle of $10\,°$, the incidence angle for which σ_0^* becomes insensitive to surface wind conditions and models. After a full turn at $12:58$ UTC, another set of $\pm 20\,°$ roll maneuvers were executed to sample σ_0^* in the along-wind direction. The dropsonde was launched around $13\,06$ UTC at $12.98\,°N$ and $52.78\,°W$. A two-way attenuation by water vapor and oxygen absorption L^2_{atm} of $0.78\,\mathrm{dB}$ was calculated using the dropsonde sounding. With an approximate distance of $700\,\mathrm{km}$, the GPM measurement closest to the calibration area was made at $10\,46\,29$ UTC at $13.67\,°N$ and $59.53\,°W$. To obtain a representative σ_0^* measurement from GPM, the swath data was averaged along-track for 10 seconds.

The measurement of σ_0^* during the across-wind roll maneuver is shown in Fig. 7, left. The blue circles mark the corresponding GPM measurements. For the HAMP MIRA data, σ_0^* was calculated using the old, estimated calibration (red dots) and the new, measured calibration (green dots). To both data sets, the model for σ_0 (Eq. 21) was fitted for the wind speed v and a

Atmos. Meas. Tech. Discuss., https://doi.org/10.5194/amt-2018-269
Manuscript under review for journal Atmos. Meas. Tech.
Discussion started: 11 October 2018

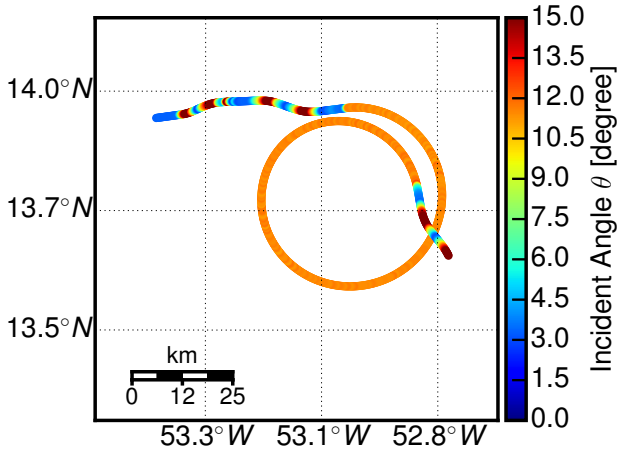

Figure 6. Overview of the flight path during the calibration maneuver with the beam incidence angle θ shown by the color-map.

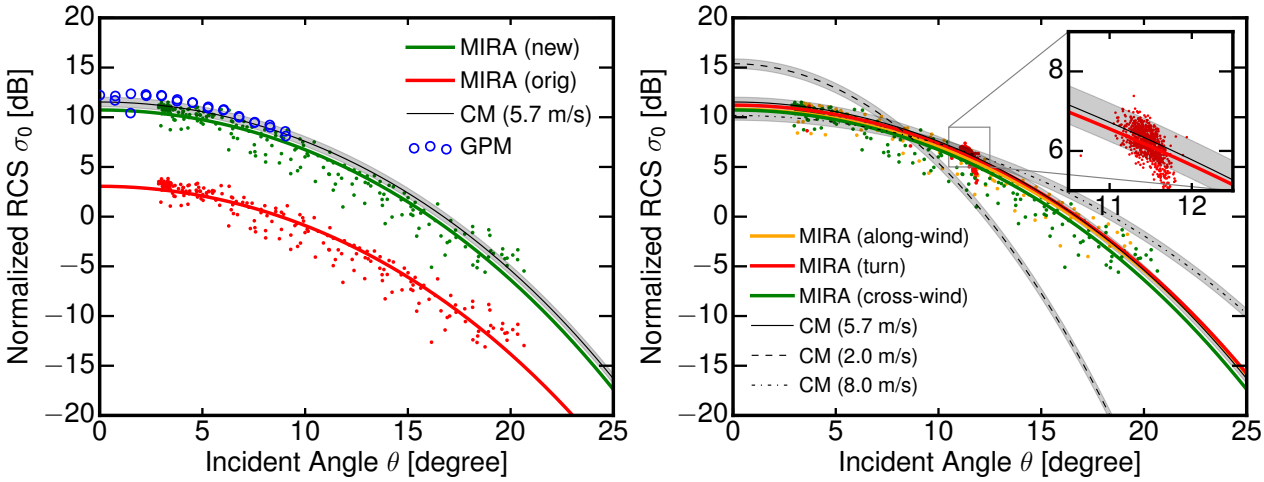

Figure 7. (left) Falloff of σ_0^* with θ measured with HAMP MIRA (red/green dots) and GPM (blue circles). The HAMP MIRA data is calculated and subsequently fitted using the old, estimated calibration (red line) and the new, measured calibration (green line). The modeled value (CM: Cox-Munk) and uncertainty of σ_0 for the actual measured wind speed from the buoy is shown by the black line and the shaded region. (right) Comparison of measured σ_0^* during the along-wind (orange) and across-wind (green) roll maneuver and during the turn (red).

possibly existing calibration offset $\Delta\sigma_0$. Additionally, σ_0 for the actual measured wind speed from the buoy is shown by the black line. The shaded region around this line illustrates the uncertainty in σ_0 due to the uncertainty in C_e $(0.85 \ldots 0.95)$. Both, modeled as well as measured σ_0 show the exponential falloff with θ corresponding to the smaller mean square slope of the ocean surface with increasing θ.

The following analysis is valid for the turn maneuver; differences between across-wind roll, turn and along-wind roll maneuver are discussed in the Fig. 7 (right) and the following paragraph. For old and new calibration, the fitted wind speed of $5.71\,\mathrm{m/s}$ agrees very well with the actual measured wind speed of $5.7\,\mathrm{m/s}$. While σ_0^* for the old calibration shows a strong underestimation of σ_0 by $\Delta\sigma_0 = -7.8\,\mathrm{dB}$, the fit for the new calibration only marginally underestimates σ_0 with $\Delta\sigma_0 = -0.2\,\mathrm{dB}$, well within the uncertainty of σ_0. Thus, the initial calibration yields $7.6\,\mathrm{dB}$ smaller values for σ_0^* when compared to the new calibration that is in good agreement with the modeled values. This observed difference also matches precisely with the $7.6\,\mathrm{dB}$ difference determined during the radiometric calibration in Sec. 3. Furthermore, the radiometric accuracy of the new calibration is supported by the GPM measurements in the vicinity. With an increasing offset $\Delta\sigma_0$ from $-0.1\,\mathrm{dB}$ to $-1\,\mathrm{dB}$ towards smaller incidence angles, GPM measured only slightly larger values within its 9° co-localized matched swath compared to the new radiometric calibration. Here, the small, increasing offset $\Delta\sigma_0$ with decreasing θ suggests a slightly lower wind speed at the GPM footprint, with more ocean surface facets pointing into the backscatter direction. The much better agreement of the new radiometric calibration with GPM is a further demonstration of its validity.

Extending this discussion, the dependence of σ_0^* on wind direction is tested in the following. In Fig. 7 on the right, σ_0^* for the across-wind roll (green), turn (red) and along-wind (orange) roll maneuver are compared with each other and fitted to the model. To put a possible directional dependence in perspective to the effect of different wind speeds, modeled σ_0 are plotted with their uncertainty for wind speeds of $2\,\mathrm{m/s}$ (dashed line), $8\,\mathrm{m/s}$ (dashed-dotted line) and the actual $5.7\,\mathrm{m/s}$ (solid line). While the across-wind results are slightly below the values of σ_0 predicted by the wind speed of the buoy by $\Delta\sigma_0 = -0.5\,\mathrm{dB}$, the along-wind results underestimate σ_0 by $\Delta\sigma_0 = -0.8\,\mathrm{dB}$. In comparison, the fit to the measurements in the turn showed the smallest offset $\Delta\sigma_0 = -0.2,\mathrm{dB}$. The closer look in the inset in Fig. 7 (right) shows a scatter with a standard deviation of $0.8\,\mathrm{dB}$. Here, the slightly higher values were measured in the downwind section of the turn; an observation that is in line with measurements by Tanelli et al. (2006). In addition, this scatter is further caused by the under-sampled point target spread function of the ocean surface with a remaining uncertainty of $1\,\mathrm{dB}$. Due to these two effects, the measured σ_0^* will be associated with an uncertainty of $1\,\mathrm{dB}$. In summary, measured σ_0^* for the new calibration agree with modeled as well as measured values within their uncertainty estimates.

5 Inter-comparison with RASTA and CloudSat

The following section will validate the preceding external calibration. To that end, we conducted common flight legs with W-Band cloud radars, like the airborne *RASTA* and the spaceborne *CloudSat*. First, possible differences between radar reflectivities at $35\,\mathrm{GHz}$ and $94\,\mathrm{GHz}$ are explored on the basis of a numerical study.

Atmos. Meas. Tech. Discuss., https://doi.org/10.5194/amt-2018-269
Manuscript under review for journal Atmos. Meas. Tech.
Discussion started: 11 October 2018

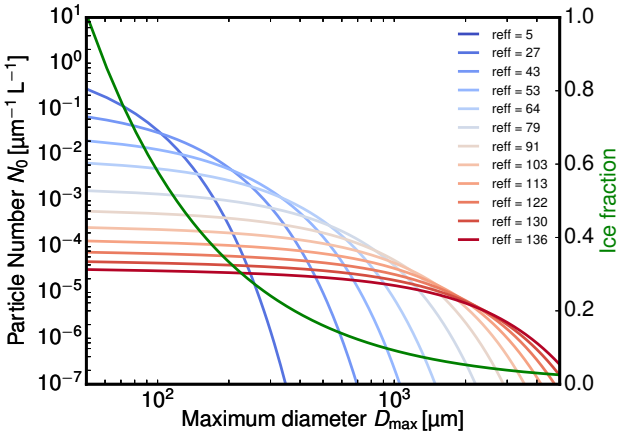

Figure 8. The ice microphysical model used during the radar reflectivity study. The particle size distribution (Delanoë et al., 2005) and the mass-size relationship (green curve) (Heymsfield et al., 2010) are based on an extensive database of airborne in situ measurements.

5.1 Model study of radar reflectivity at 35 and 94 GHz

Due to the strong dependence of radar reflectivity on ice crystal size, a realistic and well tested ice particle model (particle size distribution (PSD) and mass-size relationship) is crucial. Since PSDs are known to be highly variable (Intrieri et al., 1993), we choose the normalized PSD approach by Delanoë et al. (2014) which is based on an extensive database of airborne in situ microphysical measurements. This PSD is also a central component of the synergistic radar-lidar retrieval DARDAR (Delanoë et al., 2014) which is designated for the EarthCARE mission. Figure 8 shows this PSD as a function of melted diameter D_{eq} for the different effective ice crystal radii. The connection between the actual ice crystal and D_{eq} is described by the area-size and mass-size relationships from Heymsfield et al. (2010).

The ice crystal shape and the electromagnetic scattering properties are a further important assumption. In the following, 'Rayleigh scattering only' will be compared to Mie scattering and T-Matrix scattering theory. Mie theory is applied assuming homogeneous ice-air spheres, while the T-Matrix calculations are done for spheroids with an aspect ratio of 0.6 and same mass and area like the ice-air spheres.

The model results for a single ice crystal are shown in the left panel of Fig. 9. Here, the radar reflectivities at 35 GHz (green) and 94 GHz (red) are shown as a function of equivalent melted ice crystal diameter D_{eq} according to Rayleigh (blue), Mie (solid) and T-Matrix (dashed) theory. While the radar reflectivity derived with Rayleigh theory steadily increases with particle size to the power of six, the values start to deviate for Mie and T-Matrix theory at a D_{eq} of around $400\,\mu$m at 94 GHz and around $800\,\mu$m at 35 GHz. At D_{eq} larger than $600\,\mu$m ($1200\,\mu$m), radar reflectivity for single ice particles even decreases again for 94 GHz (resp. 35 GHz) due to Mie resonances. In a next step, this result is convolved with the normalized PSDs for different effective radii. The results for a fixed ice water content of $1\,\mathrm{gm}^{-1}$ and variable effective ice crystal radius is shown in the right panel of Fig. 9.

Atmos. Meas. Tech. Discuss., https://doi.org/10.5194/amt-2018-269
Manuscript under review for journal Atmos. Meas. Tech.
Discussion started: 11 October 2018

Atmospheric Measurement Techniques Discussions

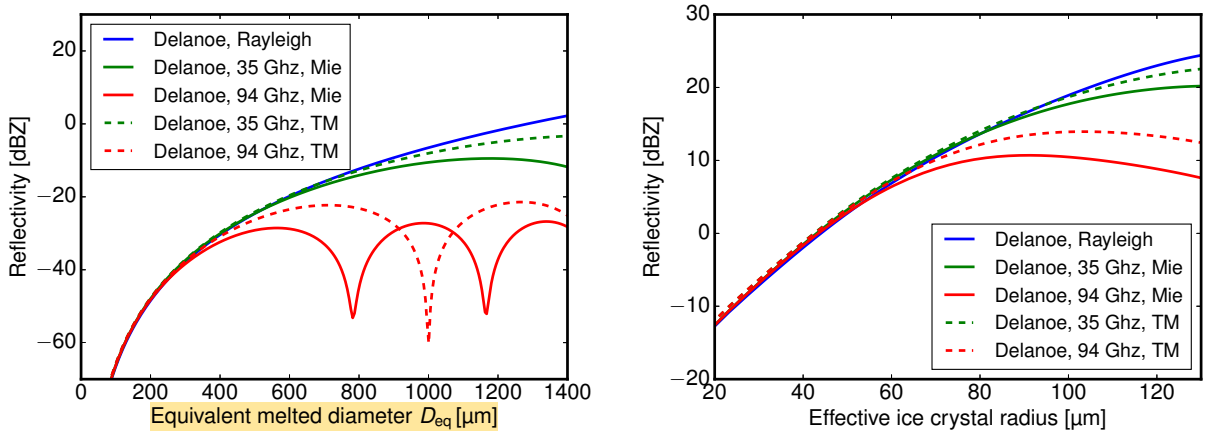

Figure 9. Modeled radar reflectivities at 35 GHz (green) and 94 GHz (red) as a function of equivalent melted ice crystal diameter D_{eq} according to Rayleigh (blue), Mie (solid) and T-Matrix (dashed) theory. While the left panel shows results for mono-disperse ice crystals, the right panel shows results for a whole distribution of ice crystals of various sizes (Fig. 8) with a fixed ice water content of $1\,\mathrm{gm}^{-1}$.

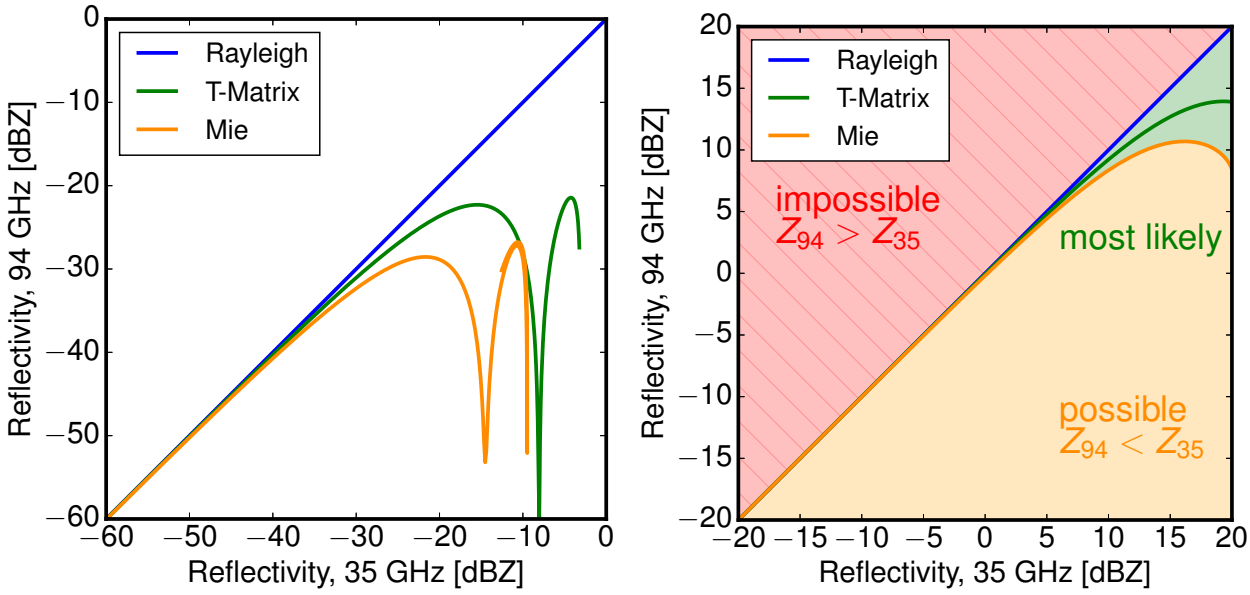

Figure 10. Comparison between modeled radar reflectivities at 94 GHz against radar reflectivities at 35 GHz according to Rayleigh (blue), Mie (solid) and T-Matrix (dashed) theory. Like in Fig. 9, the left panel shows results for mono-disperse ice crystals, while the right panel shows results for the whole distribution shown in Fig. 8. Overall, lower radar reflectivity values are almost identical, while larger radar reflectivities at 94 GHz are below the values at35 GHz.

Again, lower radar reflectivity values are almost identical, while larger radar reflectivities at 94 GHz are below the values at 35 GHz. For these realistic PSDs, radar reflectivities deviate from Rayleigh theory for effective radii larger than 80 μm at 94 GHz and 120 μm at 35 GHz. Thus, the radar reflectivity of realistic PSDs deviates at much smaller effective radii when compared to the study of single ice crystals. This is caused by a few but large ice crystals contained in each PSD, which dominate the radar reflectivity. Furthermore, the results obtained from Mie and Rayleigh theory can be considered as theoretical boundaries for more complex shaped ice crystals.

In a last study, this is used to confine the values of possible radar reflectivities when measurements at 94 GHz are compared to co-located measurements at 35 GHz. In Fig. 10 modeled radar reflectivities from Fig. 9 at 94 GHz are plotted against reflectivities at 35 GHz. Again, the blue lines show the Rayleigh result, the solid lines show result according to Mie theory and the dashed lines show results for spheroids which where obtained from T-Matrix theory. In Fig. 10 on the left, result are again shown for mono-disperse ice crystals of different sizes, while the right panel shows results for the whole ice crystal distribution for a fixed ice water content of $1\,\mathrm{gm}^{-1}$.

These theoretical calculations could be tested and validated during co-located measurements with 94 GHz cloud radar RASTA on the French Falcon research aircraft and on board the cloudsat mission.

5.2 RASTA

A coordinated flight with the French Falcon equipped with the well calibrated 94 GHz radar system RASTA and the HALO equipped with the 35 GHz radar system was performed on over Southern France and Northern Spain on 19 December 2013 between 11:00 and 11:15 UTC. Both aircraft flew in close separation of less than 5 minutes. During that leg, HALO was flying at an altitude of 13 km and passed the slower flying French FALCON at an altitude of 10 km. The SEVIRI satellite image indicated a stratiform cloud cover in the measurement area (Fig. 11). The radar measurements showed a two layer cloud structure (Fig. 12) with a lower cloud in the first half of the measurement reaching from ground to about 4 km height and an overlying cloud layer, present during the whole co-located flight, with a cloud base between about 4.5 km and 6 kmheight and an homogeneous cloud top at about 10.5 km in altitude. Thus, this coordinated flight provides an optimal measurement situation for a radar inter-comparison. Due to the close separation of the aircraft, many cloud features can be found in both measurements at the same place. On the first sight of the measurements one can suggest that the HAMP MIRA instrument shows more variability within the cloud layer. Also small-scale cloud structures are visible in the measurements made between 11:08 and 11:12 UTC. These cloud structures are not visible in the cross-section of the RASTA measurements. At first glance, the HAMP MIRA at 35 GHz is more sensitive, especially to low-lying water clouds. While the radar reflectivities of the high cirrus cloud layer is quite similar, differences become visible in precipitating clouds, but also in non-precipitating water clouds after 11:07 UTC.

For the direct comparison of radar reflectivities, the backscattered signal was corrected for gaseous attenuation by oxygen and water vapor. Like during the external calibration with the ocean surface, the gaseous absorption model for millimeter waves by Rosenkranz (1998) was used. Profiles of pressure, temperature and humidity were taken from the ECMWF Integrated Forecasting System (IFS) model. The airborne RASTA and MIRA HAMP measurements of Z are plotted against each other

Atmos. Meas. Tech. Discuss., https://doi.org/10.5194/amt-2018-269
Manuscript under review for journal Atmos. Meas. Tech.
Discussion started: 11 October 2018

Atmospheric Measurement Techniques Discussions

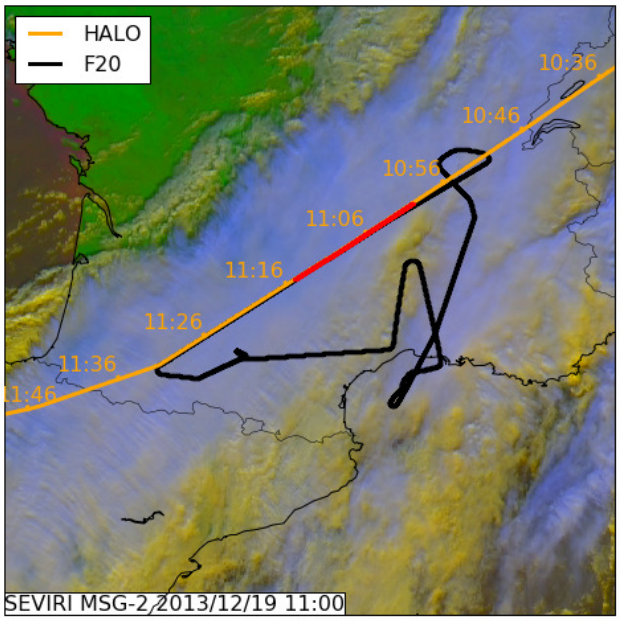

Figure 11. SEVIRI satellite image and HALO flight track for 19 December 2013. The red flight part marks the coordinated flight leg with the French Falcon and the 94 GHz airborne lidar RASTA.

in the same way as the model study shown in Fig. 10 (Fig. 13). This comparison is in good agreement with the results of the preceding model study. The direct comparison of radar reflectivities at both wavelengths shows quite similar value in the cirrus cloud layer when using the new calibration for the HAMP MIRA system. But differences become visible towards lower altitudes in precipitating clouds. As discussed in the previous model study, this can be explained with the different wavelengths used. With increasing ice crystal size, the transition from the Rayleigh scattering regime ($Z \approx D^6$) towards the Mie scattering regime ($Z \approx D^2$) first occurs at 94 GHz. The difference ΔZ between 94 and 35 GHz increases with increasing Z due to larger ice crystals at lower altitudes. The good agreement of the 35 GHz and the 94 GHz measurements in regions, where both systems should not be affected by different attenuation or scattering regimes, e.g. in the upper part of the cloud, can thus be used as an external verification of the HAMP MIRA calibration.

5.3 CloudSat

In recent years, CloudSat has been established as a reference source to compare the calibration of different ground- and airborne cloud radars (Protat et al., 2010). For this reason, the spaceborne CloudSat is used in this last comparison. Due to its reliable radiometric stability and its global coverage, CloudSat has tied the different cloud radar systems more closely together. For this reason, a CloudSat underflight performed over the subtropical North-Atlantic ocean east of Barbados on 17th August 2016 between 16:54 and 17:22 UTC (Fig. 14) is used. HALO flew aligned with the CloudSat footprint for over 450 km. During this flight, all instrument settings were identical to the calibration flight ($f_p = 6\,\mathrm{kHz}$, $\tau = 200\,\mathrm{ns}$, 1 Hz) with footprints measuring

Atmos. Meas. Tech. Discuss., https://doi.org/10.5194/amt-2018-269
Manuscript under review for journal Atmos. Meas. Tech.
Discussion started: 11 October 2018

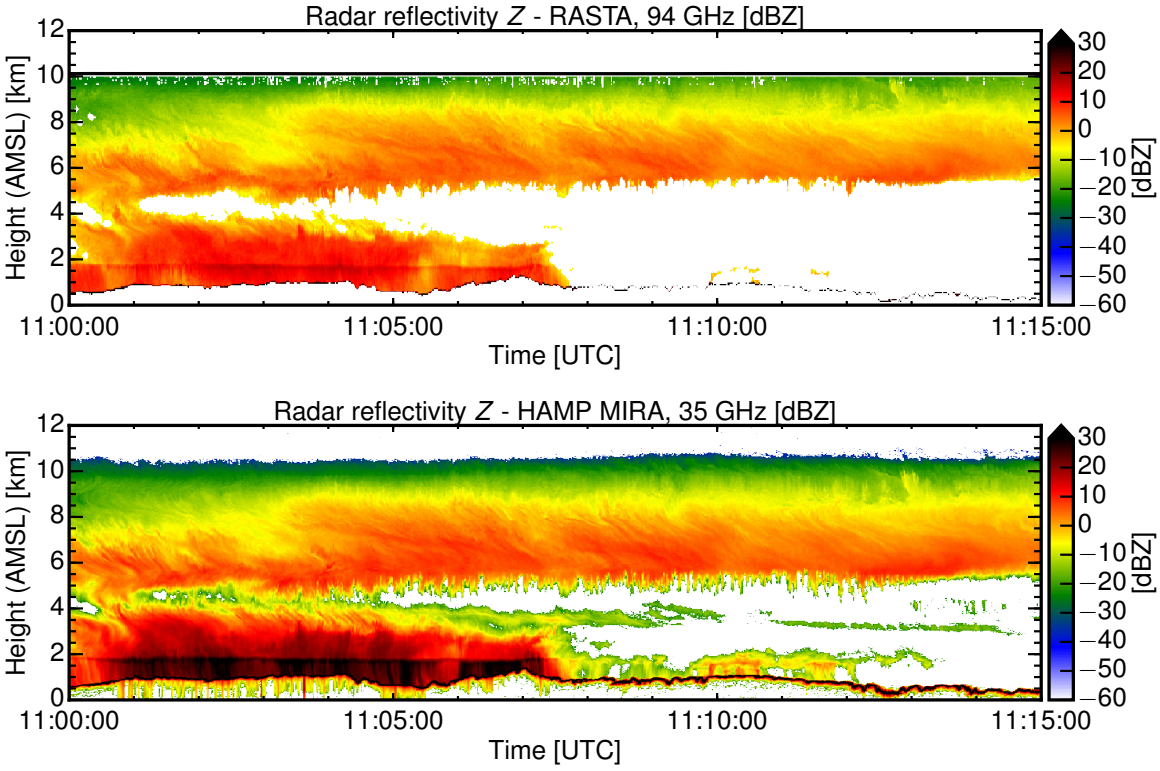

Figure 12. Radar measurements performed with the HAMP MIRA at 35 GHz (upper panel) and the RASTA system at 94 GHz (lower panel) along the coordinated flight track marked in Fig. 11.

approx 100 m in the horizontal and 30 m in the vertical. In the beginning of the underpass flight, HALO was still climbing through the cirrus layer. Coinciding with the CloudSat overpass at 17:04 UTC, the aircraft then reached the top of the cirrus layer. The overall measurement scene is characterized by inhomogeneous cirrus cloud structures with contribution of few low clouds. The first part is dominated by an extended cirrus layer. As this cirrus layer becomes thinner, the second part is composed of broken and thinner cirrus clouds and shallow, convective marine boundary layer clouds. The cirrus layer as well as the lower precipitating clouds are clearly visible from both platforms. Strong radar reflectivity gradients are more blurred in the CloudSat measurement due to the coarser horizontal (1700 m vs 200 m) and vertical (500 m vs 30 m) resolution. For this reason, cloud edges as well as internal cloud structures are better resolved in the HAMP MIRA measurements. At cloud edges, this resolution induced blurring leads to larger reflectivities while it reduces the maximum reflectivities found inside clouds. Again the measured reflectivity Z measured by CloudSat is plotted against HAMP MIRA in Fig. 13 (right). Since the scene is dominated by cirrus, the values for Z are generally lower than in the RASTA-MIRA comparison. Due to the different spatial resolutions, the scatter between air- and spaceborne platform is almost double compared to the former comparison. However,

Atmos. Meas. Tech. Discuss., https://doi.org/10.5194/amt-2018-269
Manuscript under review for journal Atmos. Meas. Tech.
Discussion started: 11 October 2018

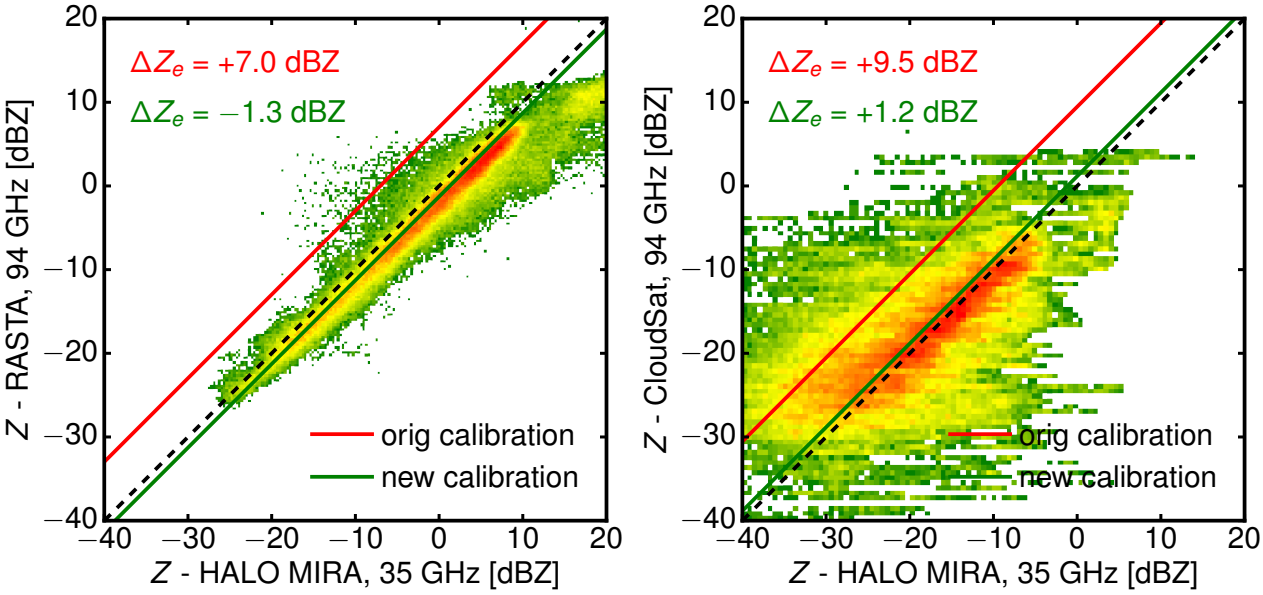

Figure 13. (left) Comparison of radar reflectivities shown in Fig. 12 measured with HAMP MIRA at 35 GHz and the airborne RASTA instrument at 94 GHz. (right) Comparison of radar reflectivities shown in Fig. 14 measured with HAMP MIRA at 35 GHz and the spaceborne CloudSat instrument at 94 GHz. The green line shows the offset fit for the new, the red line for the old HAMP MIRA calibration.

the overall agreement between the CloudSat and the HAMP MIRA measurements again validates the new calibration of the system.

6 Conclusions

In this study, we have characterized the radiometric calibration of the microwave cloud radar *HAMP MIRA*, which is installed in the belly pod section of the German research aircraft *HALO* in a fixed nadir-pointing configuration. In a first step, the respective instrument components were characterized in the lab to obtain an internal calibration of the instrument. Here, the calibration of the radar receiver gave valuable new insights about the receiver noise power and thus the receiver sensitivity. Subsequently, this component calibration was validated by using the ocean surface backscatter as a reference with known reflectivity. To this end, controlled roll maneuvers were flown during the NARVAL2 campaign in the vicinity of Barbados to sample the angular dependence of the ocean surface backscatter. The comparison with modeled backscatter values using the Cox-Munk model for non-slick ocean surfaces and measured values from the GPM satellite confirmed the internal calibration to within ±0.5 dB. In a second intercomparison study, the absolute radiometric accuracy of the internal calibration was further scrutinized during common flight legs with the airborne 94 GHz cloud radar RASTA and the spaceborne 94 GHz cloud radar CloudSat. To asses the influence of different radar wavelengths on this comparison, we first conducted a model study of radar reflectivities at 35 and 94 GHz. Using realistic ice particle size distributions, T-Matrix calculations for spheroids show almost identical radar

Atmos. Meas. Tech. Discuss., https://doi.org/10.5194/amt-2018-269
Manuscript under review for journal Atmos. Meas. Tech.
Discussion started: 11 October 2018

Atmospheric Measurement Techniques Discussions

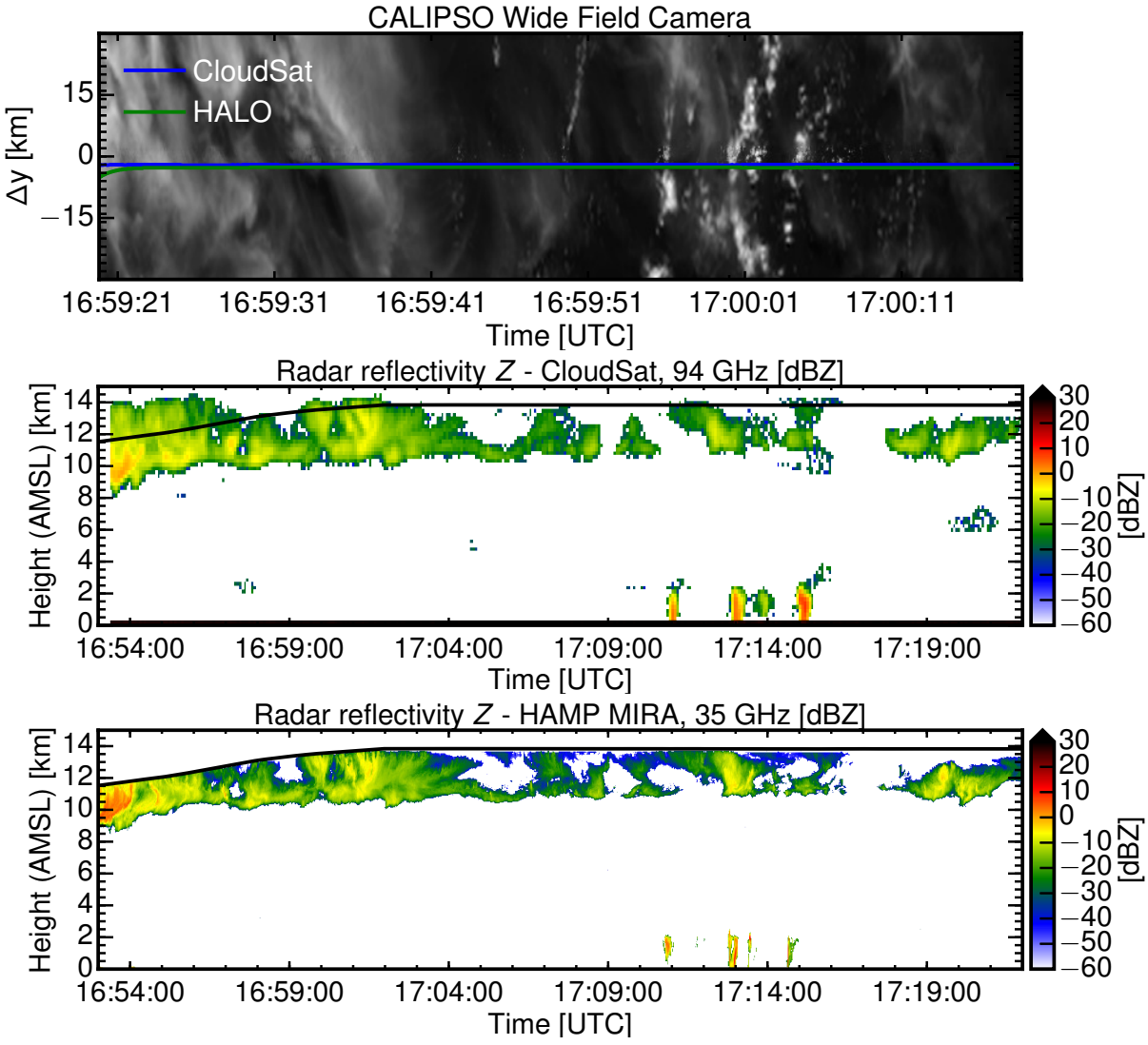

Figure 14. Radar measurements performed with the HAMP MIRA at 35 GHz (central panel) and the spaceborne CloudSat radar at 94 GHz (lower panel) along the coordinated flight track shown in the image acquired with the Wide Field Camera on CALIPSO (top panel).

reflectivities at 35 and 94 GHz for effective radii smaller 50 µm. Larger ice crystals and higher attenuation generally lead to a smaller reflectivity at 94 GHz. In this context, the intercomparison showed good agreement between the *HAMP MIRA* at 35 and the RASTA at 94 GHz with slightly lower reflectivities (−1.3 dB) for RASTA. The intercomparison with CloudSat showed slightly higher (+1.2 dB) reflectivities for CloudSat. These higher reflectivities were mostly found at cloud edges where the coarser spatial resolution of CloudSat can blur out higher reflectivities into regions with thinner reflectivity below the sensitivity of CloudSat. Concluding, these intercomparison studies showed that the absolute radiometric uncertainty is now well below the initially required accuracy of 3 dB and even brought close to the target accuracy of 1 dB.

Acknowledgements. This work was jointly supported by the German Aerospace Center (DLR), the Max Planck Society (MPI) and the German Research Foundation (DFG) through the HALO Priority Program SPP 1294, *Atmospheric and Earth System Research with the Research Aircraft HALO (High Altitude and Long Range Research Aircraft)*. Measurement equipment was kindly provided by DLR-HR. DLR-FX and its pilots are thanked for their great support during research flights. GPM data was provided by the NASA/Goddard Space Flight Center's PPS team, which develop and compute the *GPM DPR Ka vertical profile precipitation swath retrievals* (DOI: 10.5067/GPM/DPR/Ka/2A/04) as a contribution to GPM. The authors thank Oliver Lux for his internal review of the manuscript.

References

Acquistapace, C., Kneifel, S., Löhnert, U., Kollias, P., Maahn, M., and Bauer-Pfundstein, M.: Optimizing observations of drizzle onset with millimeter-wavelength radars, Atmos. Meas. Tech., 10, 1783–1802, doi:10.5194/amt-10-1783-2017, https://www.atmos-meas-tech.net/10/1783/2017/, 2017.

Apel, J. R.: An improved model of the ocean surface wave vector spectrum and its effects on radar backscatter, Journal of Geophysical Research: Oceans, 99, 16 269–16 291, doi:10.1029/94JC00846, http://onlinelibrary.wiley.com/doi/10.1029/94JC00846/abstract, 1994.

Atlas, D.: Radar Calibration: Some Simple Approaches, Bulletin of the American Meteorological Society, 83, 1313–1316, doi:10.1175/1520-0477(2002)083<1313:RCSSA>2.3.CO;2, https://journals.ametsoc.org/doi/abs/10.1175/1520-0477(2002)083%3C1313:RCSSA%3E2.3.CO;2, 2002.

Barrick, D. E., Headrick, J. M., Bogle, R. W., and Crombie, D. D.: Sea backscatter at HF: Interpretation and utilization of the echo, Proceedings of the IEEE, 62, 673–680, doi:10.1109/PROC.1974.9507, 1974.

Bauer-Pfundstein, M. and Görsdorf, U.: Target separation and classification using cloud radar Doppler-spectra, in: Proceedings 33rd Intern. Conf. on Radar Meteorology, Cairns, http://ams.confex.com/ams/33Radar/techprogram/paper_123456.htm, 2007.

Bony, S. and Dufresne, J.-L.: Marine boundary layer clouds at the heart of tropical cloud feedback uncertainties in climate models, Geophysical Research Letters, 32, L20 806, doi:10.1029/2005GL023851, http://onlinelibrary.wiley.com/doi/10.1029/2005GL023851/abstract, 2005.

Bormotov, V., Peters, G., Schünemann, K., Vavriv, D., Vinogradov, V., and Volkov, V.: 36 GHz Doppler radar for remote sensing of the atmosphere, in: Proceedings of Millennium Conference on Antenna and Propagation, Davos Switzerland, pp. 9–14, 2000.

Boucher, O., Randall, D., Artaxo, P., Bretherton, C., Feingold, G., Forster, P., Kerminen, V.-M., Kondo, Y., Liao, H., Lohmann, U., Rasch, P., Satheesh, S., Sherwood, S., Stevens, B., and Zhang, X.: Clouds and Aerosols, book section 7, pp. 571–658, Cambridge University Press, Cambridge, United Kingdom and New York, NY, USA, doi:10.1017/CBO9781107415324.016, www.climatechange2013.org, 2013.

Bouniol, D., Protat, A., Plana-Fattori, A., Giraud, M., Vinson, J.-P., and Grand, N.: Comparison of Airborne and Spaceborne 95-GHz Radar Reflectivities and Evaluation of Multiple Scattering Effects in Spaceborne Measurements, Journal of Atmospheric and Oceanic Technology, 25, 1983–1995, doi:10.1175/2008JTECHA1011.1, http://journals.ametsoc.org/doi/abs/10.1175/2008JTECHA1011.1, 2008.

Brown, G. S.: Quasi-Specular Scattering from the Air-Sea Interface, in: Surface Waves and Fluxes, Environmental Fluid Mechanics, pp. 1–39, Springer, Dordrecht, https://link.springer.com/chapter/10.1007/978-94-009-0627-3_1, dOI: 10.1007/978-94-009-0627-3_1, 1990.

Caylor, I. J., Heymsfield, G. M., Meneghini, R., and Miller, L. S.: Correction of Sampling Errors in Ocean Surface Cross-Sectional Estimates from Nadir-Looking Weather Radar, Journal of Atmospheric and Oceanic Technology, 14, 203–210, doi:10.1175/1520-0426(1997)014<0203:COSEIO>2.0.CO;2, http://journals.ametsoc.org/doi/full/10.1175/1520-0426(1997)014%3C0203%3ACOSEIO%3E2.0.CO%3B2, 1997.

Caylor, I. J. H.: NASA ER-2 Doppler radar reflectivity calibration for the CAMEX project, Tech. rep., Goddard Space Flight Center. Greenbelt, Maryland, https://ntrs.nasa.gov/search.jsp?R=19940033279, 1994.

Chen, T., Zhang, Y., and Rossow, W.: Sensitivity of atmospheric radiative heating rate profiles to variations of cloud layer overlap, Journal of Climate, 13, 2941–2959, 2000.

Cox, C. and Munk, W.: Measurement of the roughness of the sea surface from photographs of the sun's glitter, Journal of the Optical Society of America, 44, 838–850, 1954.

Delanoë, J. and Hogan, R. J.: A variational scheme for retrieving ice cloud properties from combined radar, lidar, and infrared radiometer, Journal of Geophysical Research, 113, D07 204, http://www.agu.org/pubs/crossref/2008/2007JD009000.shtml, 2008.

Delanoë, J., Protat, A., Testud, J., Bouniol, D., Heymsfield, A. J., Bansemer, A., Brown, P. R. A., and Forbes, R. M.: Statistical properties of the normalized ice particle size distribution, Journal of Geophysical Research: Atmospheres, 110, D10 201, doi:10.1029/2004JD005405, http://onlinelibrary.wiley.com/doi/10.1029/2004JD005405/abstract, 2005.

Delanoë, J. M. E., Heymsfield, A. J., Protat, A., Bansemer, A., and Hogan, R. J.: Normalized particle size distribution for remote sensing application, Journal of Geophysical Research: Atmospheres, 119, 4204–4227, doi:10.1002/2013JD020700, http://onlinelibrary.wiley.com/doi/10.1002/2013JD020700/abstract, 2014.

Deng, M., Mace, G. G., Wang, Z., and Okamoto, H.: Tropical Composition, Cloud and Climate Coupling Experiment validation for cirrus cloud profiling retrieval using CloudSat radar and CALIPSO lidar, Journal of Geophysical Research: Atmospheres, 115, D00J15, doi:10.1029/2009JD013104, http://onlinelibrary.wiley.com/doi/10.1029/2009JD013104/abstract, 2010.

Donovan, D. P., van Lammeren, A., Hogan, R., Russchenberg, H., Apituley, A., Francis, P., Testud, J., Pelon, J., Quante, M., and Agnew, J.: Combined radar and lidar cloud remote sensing: Comparison with IR radiometer and in-situ measurements, Phys. Chem. Earth (B), 25, 1049–1055, 2000.

Doviak, R. J. and Zrnić, D.: Receiver Bandwidth Effect on Reflectivity and Doppler Velocity Estimates, Journal of Applied Meteorology, 18, 69–76, doi:10.1175/1520-0450(1979)018<0069:RBEORA>2.0.CO;2, http://journals.ametsoc.org/doi/abs/10.1175/1520-0450%281979%29018%3C0069%3ARBEORA%3E2.0.CO%3B2, 1979.

Doviak, R. J. and Zrnić, D. S.: Doppler Radar and Weather Observations, Dover Publications, 1993.

Durden, S. L., Im, E., Li, F. K., Ricketts, W., Tanner, A., and Wilson, W.: ARMAR: An Airborne Rain-Mapping Radar, Journal of Atmospheric and Oceanic Technology, 11, 727–737, doi:10.1175/1520-0426(1994)011<0727:AAARMR>2.0.CO;2, http://journals.ametsoc.org/doi/abs/10.1175/1520-0426%281994%29011%3C0727%3AAAAARMR%3E2.0.CO%3B2, 1994.

Ewald, F., Winkler, C., and Zinner, T.: Reconstruction of cloud geometry using a scanning cloud radar, Atmos. Meas. Tech., 8, 2491–2508, doi:10.5194/amt-8-2491-2015, http://www.atmos-meas-tech.net/8/2491/2015/, 2015.

Freilich, M. H. and Vanhoff, B. A.: The Relationship between Winds, Surface Roughness, and Radar Backscatter at Low Incidence Angles from TRMM Precipitation Radar Measurements, Journal of Atmospheric and Oceanic Technology, 20, 549–562, doi:10.1175/1520-0426(2003)20<549:TRBWSR>2.0.CO;2, http://journals.ametsoc.org/doi/abs/10.1175/1520-0426%282003%2920%3C549%3ATRBWSR%3E2.0.CO%3B2, 2003.

Görsdorf, U., Lehmann, V., Bauer-Pfundstein, M., Peters, G., Vavriv, D., Vinogradov, V., and Volkov, V.: A 35-GHz Polarimetric Doppler Radar for Long-Term Observations of Cloud Parameters—Description of System and Data Processing, Journal of Atmospheric and Oceanic Technology, 32, 675–690, doi:10.1175/JTECH-D-14-00066.1, http://journals.ametsoc.org/doi/abs/10.1175/JTECH-D-14-00066.1, 2015.

Haimov, S. and Rodi, A.: Fixed-Antenna Pointing-Angle Calibration of Airborne Doppler Cloud Radar, Journal of Atmospheric and Oceanic Technology, 30, 2320–2335, doi:10.1175/JTECH-D-12-00262.1, http://journals.ametsoc.org/doi/abs/10.1175/JTECH-D-12-00262.1, 2013.

Handwerker, J. and Miller, M. A.: Intercomparison of measurements obtained by vertically pointing collocated 95 GHz and 35.5 GHz cloud radars, in: Proc. Fifth European Conference on Radar in Meteorology and Hydrology, http://pd95b2c0f.dip0.t-ipconnect.de/literature/erad2008-Handwerker_35-95_ext.pdf, 2008.

Henderson, D. S., L'Ecuyer, T., Stephens, G., Partain, P., and Sekiguchi, M.: A Multisensor Perspective on the Radiative Impacts of Clouds and Aerosols, Journal of Applied Meteorology and Climatology, 52, 853–871, doi:10.1175/JAMC-D-12-025.1, https://journals.ametsoc.org/doi/abs/10.1175/JAMC-D-12-025.1, 2012.

Hennemuth, B., Weiss, A., Bösenberg, J., Jacob, D., Linné, H., Peters, G., and Pfeifer, S.: Quality assessment of water cycle parameters in REMO by radar-lidar synergy, Atmos. Chem. Phys., 8, 287–308, doi:10.5194/acp-8-287-2008, https://www.atmos-chem-phys.net/8/287/2008/, 2008.

Heymsfield, A., Bansemer, A., Field, P., Durden, S., Stith, J., Dye, J., Hall, W., and Grainger, C.: Observations and parameterizations of particle size distributions in deep tropical cirrus and stratiform precipitating clouds: Results from in situ observations in TRMM field campaigns, Journal of the Atmospheric Sciences, 59, 2010.

Heymsfield, G. M., Bidwell, S. W., Caylor, I. J., Ameen, S., Nicholson, S., Boncyk, W., Miller, L., Vandemark, D., Racette, P. E., and Dod, L. R.: The EDOP Radar System on the High-Altitude NASA ER-2 Aircraft, Journal of Atmospheric and Oceanic Technology, 13, 795–809, doi:10.1175/1520-0426(1996)013<0795:TERSOT>2.0.CO;2, http://journals.ametsoc.org/doi/abs/10.1175/1520-0426%281996%29013%3C0795%3ATERSOT%3E2.0.CO%3B2, 1996.

Hong, Y., Liu, G., and Li, J.-L. F.: Assessing the Radiative Effects of Global Ice Clouds Based on CloudSat and CALIPSO Measurements, Journal of Climate, 29, 7651–7674, doi:10.1175/JCLI-D-15-0799.1, http://journals.ametsoc.org/doi/abs/10.1175/JCLI-D-15-0799.1, 2016.

Horie, H. and Takahashi, N.: External calibration method using sea surface scattering for satelliteborne W-band cloud profiling radar, in: Proc. of ISPRS, vol. 38, pp. 160–163, http://www.tric.u-tokai.ac.jp/isprscom8/tc8/TC8_CD/headline/NICT%20special%20Session%20-%202/NTS25_20100608144300.pdf, 2010.

Horie, H., Iguchi, T., Hanado, H., Kuroiwa, H., Okamoto, H., and Kumagai, H.: Development of a 95-GHz Airborne Cloud Profiling Radar (SPIDER) –Technical Aspects–, IEICE TRANSACTIONS on Communications, E83-B, 2010–2020, http://search.ieice.org/bin/summary.php?id=e83-b_9_2010&category=B&year=2000&lang=E&abst=, 2000.

Horie, H., Kuroiwa, H., and Kumagai, H.: Near nadir scattering properties at W-band frequency for the sea surface, in: IGARSS 2004. 2004 IEEE International Geoscience and Remote Sensing Symposium, vol. 3, pp. 1742–1745 vol.3, doi:10.1109/IGARSS.2004.1370669, 2004.

Hou, A. Y., Kakar, R. K., Neeck, S., Azarbarzin, A. A., Kummerow, C. D., Kojima, M., Oki, R., Nakamura, K., and Iguchi, T.: The Global Precipitation Measurement Mission, Bulletin of the American Meteorological Society, 95, 701–722, doi:10.1175/BAMS-D-13-00164.1, https://journals.ametsoc.org/doi/full/10.1175/BAMS-D-13-00164.1, 2013.

Illingworth, A. J., Hogan, R. J., O'Connor, E. J., Bouniol, D., Delanoë, J., Pelon, J., Protat, A., Brooks, M. E., Gaussiat, N., Wilson, D. R., Donovan, D. P., Baltink, H. K., van Zadelhoff, G.-J., Eastment, J. D., Goddard, J. W. F., Wrench, C. L., Haeffelin, M., Krasnov, O. A., Russchenberg, H. W. J., Piriou, J.-M., Vinit, F., Seifert, A., Tompkins, A. M., and Willén, U.: Cloudnet Continuous Evaluation of Cloud Profiles in Seven Operational Models Using Ground-Based Observations, Bulletin of the American Meteorological Society, 88, 883–898, doi:10.1175/BAMS-88-6-883, http://journals.ametsoc.org/doi/abs/10.1175/BAMS-88-6-883, 2007.

Illingworth, A. J., Barker, H. W., Beljaars, A., Ceccaldi, M., Chepfer, H., Clerbaux, N., Cole, J., Delanoë, J., Domenech, C., Donovan, D. P., Fukuda, S., Hirakata, M., Hogan, R. J., Huenerbein, A., Kollias, P., Kubota, T., Nakajima, T., Nakajima, T. Y., Nishizawa, T., Ohno, Y., Okamoto, H., Oki, R., Sato, K., Satoh, M., Shephard, M. W., Velázquez-Blázquez, A., Wandinger, U., Wehr, T., and van Zadelhoff, G.-J.: The EarthCARE Satellite: The Next Step Forward in Global Measurements of Clouds, Aerosols, Precipitation, and Radiation, Bulletin of the American Meteorological Society, 96, 1311–1332, doi:10.1175/BAMS-D-12-00227.1, http://journals.ametsoc.org/doi/abs/10.1175/BAMS-D-12-00227.1, 2014.

Intrieri, J. M., Stephens, G. L., Eberhard, W. L., and Uttal, T.: A Method for Determining Cirrus Cloud Particle Sizes Using Lidar and Radar Backscatter Technique, Journal of Applied Meteorology, 32, 1074–1082, doi:10.1175/1520-0450(1993)032<1074:AMFDCC>2.0.CO;2, http://journals.ametsoc.org/doi/abs/10.1175/1520-0450(1993)032%3C1074%3AAMFDCC%3E2.0.CO%3B2, 1993.

Jackson, F. C. W.: Sea surface mean square slope from Ku-band backscatter data, Journal of Geophysical Research, https://ntrs.nasa.gov/search.jsp?R=19920066044, 1992.

Klein, L. and Swift, C.: An improved model for the dielectric constant of sea water at microwave frequencies, IEEE Journal of Oceanic Engineering, 2, 104–111, doi:10.1109/JOE.1977.1145319, 1977.

Krautstrunk, M. and Giez, A.: The Transition From FALCON to HALO Era Airborne Atmospheric Research, in: Atmospheric Physics, edited by Schumann, U., Research Topics in Aerospace, pp. 609–624, Springer Berlin Heidelberg, http://link.springer.com/chapter/10.1007/978-3-642-30183-4_37, 2012.

Li, L., Heymsfield, G. M., Racette, P. E., Tian, L., and Zenker, E.: A 94-GHz Cloud Radar System on a NASA High-Altitude ER-2 Aircraft, Journal of Atmospheric and Oceanic Technology, 21, 1378–1388, doi:10.1175/1520-0426(2004)021<1378:AGCRSO>2.0.CO;2, http://journals.ametsoc.org/doi/abs/10.1175/1520-0426%282004%29021%3C1378%3AAGCRSO%3E2.0.CO%3B2, 2004.

Li, L., Heymsfield, G. M., Tian, L., and Racette, P. E.: Measurements of Ocean Surface Backscattering Using an Airborne 94-GHz Cloud Radar—Implication for Calibration of Airborne and Spaceborne W-Band Radars, Journal of Atmospheric and Oceanic Technology, 22, 1033–1045, doi:10.1175/JTECH1722.1, http://journals.ametsoc.org/doi/abs/10.1175/JTECH1722.1, 2005a.

Li, Z., Cribb, M., Chang, F.-L., Trishchenko, A., and Luo, Y.: Natural variability and sampling errors in solar radiation measurements for model validation over the Atmospheric Radiation Measurement Southern Great Plains region, Journal of Geophysical Research, 110, doi:10.1029/2004JD005 028, 2005b.

Lonitz, K., Stevens, B., Nuijens, L., Sant, V., Hirsch, L., and Seifert, A.: The Signature of Aerosols and Meteorology in Long-Term Cloud Radar Observations of Trade Wind Cumuli, Journal of the Atmospheric Sciences, 72, 4643–4659, doi:10.1175/JAS-D-14-0348.1, http://journals.ametsoc.org/doi/abs/10.1175/JAS-D-14-0348.1, 2015.

Maahn, M. and Kollias, P.: Improved Micro Rain Radar snow measurements using Doppler spectra post-processing, Atmos. Meas. Tech., 5, 2661–2673, doi:10.5194/amt-5-2661-2012, https://www.atmos-meas-tech.net/5/2661/2012/, 2012.

Masuko, H., Okamoto, K., Shimada, M., and Niwa, S.: Measurement of microwave backscattering signatures of the ocean surface using X band and Ka band airborne scatterometers, Journal of Geophysical Research: Oceans (1978–2012), 91, 13 065–13 083, doi:10.1029/JC091iC11p13065, http://onlinelibrary.wiley.com/doi/10.1029/JC091iC11p13065/abstract, 1986.

Mech, M., Orlandi, E., Crewell, S., Ament, F., Hirsch, L., Hagen, M., Peters, G., and Stevens, B.: HAMP – the microwave package on the High Altitude and LOng range research aircraft (HALO), Atmos. Meas. Tech., 7, 4539–4553, doi:10.5194/amt-7-4539-2014, http://www.atmos-meas-tech.net/7/4539/2014/, 2014.

Meissner, T. and Wentz, F. J.: The complex dielectric constant of pure and sea water from microwave satellite observations, IEEE Transactions on Geoscience and Remote Sensing, 42, 1836–1849, doi:10.1109/TGRS.2004.831888, 2004.

Myagkov, A., Seifert, P., Wandinger, U., Bühl, J., and Engelmann, R.: Relationship between temperature and apparent shape of pristine ice crystals derived from polarimetric cloud radar observations during the ACCEPT campaign, Atmos. Meas. Tech., 9, 3739–3754, doi:10.5194/amt-9-3739-2016, http://www.atmos-meas-tech.net/9/3739/2016/, 2016.

Nouguier, F., Mouche, A., Rascle, N., Chapron, B., and Vandemark, D.: Analysis of Dual-Frequency Ocean Backscatter Measurements at Ku- and Ka-Bands Using Near-Nadir Incidence GPM Radar Data, IEEE Geoscience and Remote Sensing Letters, 13, 1310–1314, doi:10.1109/LGRS.2016.2583198, 2016.

Plant, W. J.: A stochastic, multiscale model of microwave backscatter from the ocean, Journal of Geophysical Research: Oceans, 107, 3120, doi:10.1029/2001JC000909, http://onlinelibrary.wiley.com/doi/10.1029/2001JC000909/abstract, 2002.

Protat, A., Pelon, J., Grand, N., Delville, P., Laborie, P., Vinson, J.-P., Bouniol, D., Bruneau, D., Chepfer, H., Delanoë, J., Haeffelin, M., Noel, V., and Tinel, C.: The Rali project: combining a radar and a lidar for the study of weakly-precipitating clouds, http://hdl.handle.net/2042/36076, 2004.

Protat, A., Bouniol, D., Delanoë, J., O'Connor, E., May, P. T., Plana-Fattori, A., Hasson, A., Görsdorf, U., and Heymsfield, A. J.: Assessment of Cloudsat Reflectivity Measurements and Ice Cloud Properties Using Ground-Based and Airborne Cloud Radar Observations, Journal of Atmospheric and Oceanic Technology, 26, 1717–1741, doi:10.1175/2009JTECHA1246.1, http://journals.ametsoc.org/doi/abs/10.1175/2009JTECHA1246.1, 2009.

Protat, A., Bouniol, D., O'Connor, E. J., Klein Baltink, H., Verlinde, J., and Widener, K.: CloudSat as a Global Radar Calibrator, Journal of Atmospheric and Oceanic Technology, 28, 445–452, doi:10.1175/2010JTECHA1443.1, http://journals.ametsoc.org/doi/abs/10.1175/2010JTECHA1443.1, 2010.

Protat, A., Delanoë, J., Strapp, J. W., Fontaine, E., Leroy, D., Schwarzenboeck, A., Lilie, L., Davison, C., Dezitter, F., Grandin, A., and Weber, M.: The Measured Relationship between Ice Water Content and Cloud Radar Reflectivity in Tropical Convective Clouds, Journal of Applied Meteorology and Climatology, 55, 1707–1729, doi:10.1175/JAMC-D-15-0248.1, http://journals.ametsoc.org/doi/abs/10.1175/JAMC-D-15-0248.1, 2016.

Ray, P. S.: Broadband complex refractive indices of ice and water, Applied Optics, 11, 1836, doi:10.1364/AO.11.001836, http://adsabs.harvard.edu/abs/1972ApOpt..11.1836R, 1972.

Rosenkranz, P. W.: Water vapor microwave continuum absorption: A comparison of measurements and models, Radio Science, 33, 919–928, doi:10.1029/98RS01182, 1998.

Sadowy, G. A., Berkun, A. C., Chun, W., Im, E., and Durden, S. L.: Development of an advanced airborne precipitation radar, Microwave Journal, 46, 84–86, https://airbornescience.nasa.gov/sites/default/files/documents/pr2-mwj.pdf, 2003.

Sekelsky, S. M.: Near-Field Reflectivity and Antenna Boresight Gain Corrections for Millimeter-Wave Atmospheric Radars, Journal of Atmospheric and Oceanic Technology, 19, 468–477, doi:10.1175/1520-0426(2002)019<0468:NFRAAB>2.0.CO;2, http://journals.ametsoc.org/doi/full/10.1175/1520-0426(2002)019%3C0468%3ANFRAAB%3E2.0.CO%3B2, 2002.

Stephens, G., Vane, D., Boain, R., Mace, G., Sassen, K., Wang, Z., Illingworth, A., O'Connor, E., Rossow, W., Durden, S., Miller, S., Austin, R., Benedetti, A., Mitrescu, C., and the CloudSat Science Team: The CloudSat mission and the A-train, Bull Amer Met Soc, 83, 1771–1790, 2002.

Stubenrauch, C. J., Rossow, W. B., Kinne, S., Ackerman, S., Cesana, G., Chepfer, H., Di Girolamo, L., Getzewich, B., Guignard, A., Heidinger, A., Maddux, B. C., Menzel, W. P., Minnis, P., Pearl, C., Platnick, S., Poulsen, C., Riedi, J., Sun-Mack, S., Walther, A., Winker, D., Zeng, S., and Zhao, G.: Assessment of Global Cloud Datasets from Satellites: Project and Database Initiated by the GEWEX Radiation Panel, Bulletin of the American Meteorological Society, 94, 1031–1049, doi:10.1175/BAMS-D-12-00117.1, http://journals.ametsoc.org/doi/abs/10.1175/BAMS-D-12-00117.1, 2013.

Tanelli, S., Durden, S. L., and Im, E.: Simultaneous Measurements of Ku- and Ka-Band Sea Surface Cross Sections by an Airborne Radar, IEEE Geoscience and Remote Sensing Letters, 3, 359–363, doi:10.1109/LGRS.2006.872929, http://adsabs.harvard.edu/abs/2006IGRSL..3..359T, 2006.

Tanelli, S., Durden, S. L., Im, E., Pak, K. S., Reinke, D. G., Partain, P., Haynes, J. M., and Marchand, R. T.: CloudSat's Cloud Profiling Radar After Two Years in Orbit: Performance, Calibration, and Processing, IEEE Transactions on Geoscience and Remote Sensing, 46, 3560–3573, doi:10.1109/TGRS.2008.2002030, 2008.

Valenzuela, G. R.: Theories for the interaction of electromagnetic and oceanic waves — A review, Boundary-Layer Meteorology, 13, 61–85, doi:10.1007/BF00913863, https://link.springer.com/article/10.1007/BF00913863, 1978.

Vavriv, D. M., Volkov, V. A., Bormotov, V. N., Vynogradov, V. V., Kozhyn, R. V., Trush, B. V., Belikov, A. A., and Semenyuta, V. Y.: Millimeter-wave radars for environmental studies, Telecommunications and Radio Engineering, 61, http://www.dl.begellhouse.com/journals/0632a9d54950b268,51ed66f435ca9ff2,1890baa935ca8045.html, 2004.

Wu, J.: Mean square slopes of the wind-disturbed water surface, their magnitude, directionality, and composition, Radio Science, 25, 37–48, doi:10.1029/RS025i001p00037, http://onlinelibrary.wiley.com/doi/10.1029/RS025i001p00037/abstract, 1990.

Zhao, C., Xie, S., Klein, S. A., Protat, A., Shupe, M. D., McFarlane, S. A., Comstock, J. M., Delanoë, J., Deng, M., Dunn, M., Hogan, R. J., Huang, D., Jensen, M. P., Mace, G. G., McCoy, R., O'Connor, E. J., Turner, D. D., and Wang, Z.: Toward understanding of differences in current cloud retrievals of ARM ground-based measurements, Journal of Geophysical Research: Atmospheres, 117, D10 206, doi:10.1029/2011JD016792, http://onlinelibrary.wiley.com/doi/10.1029/2011JD016792/abstract, 2012.